Dissertations and Theses

1-2015

Cubesat Wakes in the Earth's Ionosphere

Robert M. Albarran II
Embry-Riddle Aeronautical University - Daytona Beach

Follow this and additional works at: https://commons.erau.edu/edt

Part of the Space Vehicles Commons

CUBESAT WAKES IN THE EARTH'S IONOSPHERE

BY

ROBERT M. ALBARRAN II

A Thesis

Submitted to the Department of Physical Sciences

and the Committee on Graduate Studies

In partial fulfillment of the requirements

for the degree of

Master in Science in Engineering Physics

01/2015

Embry-Riddle Aeronautical University

Daytona Beach, Florida
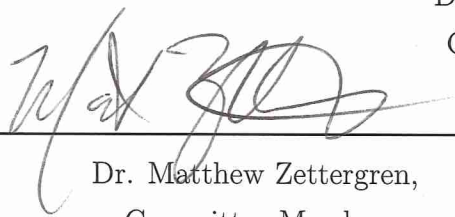
CUBESAT WAKES IN THE EARTH'S IONOSPHERE

by

Robert M. Albarran II

This thesis was prepared under the direction of the candidate's Thesis Committee Chair, Dr. Aroh Barjatya, and has been approved by the Thesis Committee. It was submitted to the Department of Physical Sciences in partial fulfillment of the requirements of the degree of

Master of Science in Engineering Physics

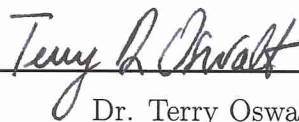THESIS COMMITTEE:

Dr. Aroh Barjatya,
Committee Chair

Dr. Matthew Zettergren,
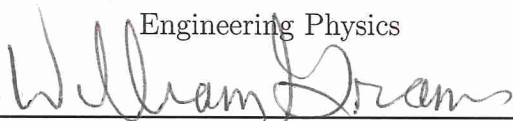Committee Member

---
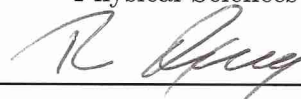
Dr. Charles Lee,
Committee Member

Dr. Peter Erdman,
Graduate Program Chair,
Engineering Physics

Dr. Terry Oswalt,
Department Chair,
Physical Sciences

Dr. William Grams,
Dean, College of Arts and Sciences

Dr. Robert Oxley,
Associate V.P. for Academics

Abstract

Space exploration is currently being revolutionized by the advent of the CubeSat: 10cm cubed satellites that typically deploy in constellations for less than $100,000. Spacecraft instrumentation design must be redefined to abide by the compact CubeSat payload. Furthermore, the CubeSat dimension must be considered with respect to characteristic length scales of the space plasma environment, namely, the Debye length. Although spacecraft-plasma interactions- surface charging, plasma sheaths and wakes- have been well-studied for larger satellites, they are less understood for CubeSats.

The Dynamic Ionosphere CubeSat Experiment (DICE) is a 1.5U CubeSat which recently ended its mission. DICE carried two fixed-bias Langmuir probes operating in the ion saturation regime that extended 180° apart from each other on scissor booms. Since the CubeSat was tumbling without proper attitude control, the plasma density measurements rendered by the probes were spin-modulated– as the probes moved in and out of the spacecraft wake, the relative density detected was modulated. Researchers who analyze such spin-modulated data routinely discard the lower density measurements from the spin-cycle attributing it to a density depletion in the spacecraft wake. It is traditionally assumed that the higher density measurement within a spin-cycle is being made outside the wake and thus is a better proxy of the ambient plasma density. While such assumptions might be true for larger spacecraft, this thesis investigates if it holds true for CubeSats in Earth's ionosphere.

The Spacecraft Plasma Interaction System (SPIS) is a widely recognized and powerful particle-in-cell (PIC) simulation tool. In this thesis, SPIS is employed to investigate the manner that a CubeSat interacts with the plasma environment when electron thermal velocities vastly exceed the spacecraft velocity which, in turn, vastly exceeds ion thermal velocities. These are so-called "meso-thermal" conditions which are typical of plasmas in Earth's ionosphere. Analysis of surface charging shows that the CubeSat abides by the thick-sheath model of Langmuir probes– the CubeSat dimension of 10 cm is comparable to the sheath thickness. More importantly, it is shown that, contrary to popular belief, there is a density enhancement in the CubeSat wake. SPIS results show that a negatively charged CubeSat in

meso-thermal conditions creates an ion focus region in the far-wake. Finally, an independent code, written in MATLAB, is developed which verifies that this feature is a direct result of the CubeSat behaving like a Langmuir probe in the thick-sheath model.

The work performed towards this thesis cautions the community towards assuming Cube-Sats to have density depletions in their wakes, and stresses the necessity of having an accurate attitude solution to derive ambient plasma densities from spin-modulated Langmuir probe measurements. Ultimately, this work may inspire new perspectives in Langmuir probe development and data analysis for CubeSats.

Acknowledgments

I primarily thank my project advisor, Aroh Barjatya, for making this study possible. I would also like to acknowledge Jeff Klenzing, Doug Rowland, Robert F. Pfaff, David L. Cooke, Shu T. Lai, Juan R. Sanmartin, Henry Garrett, the SPIS development team and countless others in the spacecraft charging and space plasma physics community for their support. Finally, I thank my family and friends for believing in me. This thesis is dedicated to my grandfathers.

Contents

List of Tables

List of Figures

Chapter 1

INTRODUCTION

Earth's space environment consists of plasma– a quasi-neutral system of generally non-relativistic positively charged ions and free electrons. Charged particles in a plasma collectively respond to external electromagnetic fields and interact amongst themselves by internally generated electromagnetic fields. Single particle motions in the microscopic perspective of plasma are governed by electromagnetic forces and characterized by Newtonian mechanics. Alternatively, the macroscopic perspective of plasma exhibits both fluid and electromagnetic behavior as illustrated by magnetohydrodynamic (MHD) relations [Cravens, 1997], [Gombosi, 1998], [Shunk and Nagy, 2009]. In the numerical and analytical treatment of CubeSat-plasma interactions, an approximately meso-scale perspective of the space plasma is adequately employed in the terrestrial ionosphere.

The plasma frequency, ω_p, is the frequency at which two equal and opposite surface charge densities oscillate due to electrostatic interaction. It encodes information about the electrostatic properties of the system which may include both electron and positively charged ion distributions. The electron plasma frequency is

$$\omega_{pe} \equiv \left(\frac{n_e e^2}{\epsilon_0 m_e} \right)^{1/2}, \tag{1.1}$$

where n_e is the electron number density, e is the elementary unit of charge, ϵ_0 is the electric permittivity in a vacuum and m_e is the electron mass [Cravens, 1997]. The plasma frequency is a significant parameter when modeling plasma dynamics; generally, the motion time-step must be comparable or less than the plasma frequency inverse [Thiebault et al., 2013].

For mobile positively charged ions of mass m_i in the system, an ion plasma frequency exists:

1

$$\omega_{pi} \equiv \left(\frac{n_i e^2}{\epsilon_0 m_i} \right)^{1/2}, \tag{1.2}$$

where $n_i = n_e$ is the ion number density according to quasi-neutrality. These two particle frequencies add in quadrature to construct the plasma frequency:

$$\omega_p = \left(\omega_{pe}^2 + \omega_{pi}^2 \right)^{1/2}. \tag{1.3}$$

Since $m_i \gg m_e$ for ions, $\omega_{pe} \approx \omega_p$ is generally a suitable approximation [Cravens, 1997].

A positive charged particle, q_0, centered in a plasma system with equal electron and ion number densities, n_0 (i.e. $n_e = n_i = n_0$) will reconfigure its environment such that, in its vicinity, the electron density will exceed the background density, n_0, while the ion density will decrease below nominal. Far from q_0, $n_e \to n_i$ (for thermal equilibrium) in the well-known plasma phenomenon known as quasi-neutrality. The potential field due to q_0 shows an e-fold decrease with distance from q_0, r, at a λ_D length scale:

$$\phi(r) = \frac{1}{4\pi\epsilon_0} \frac{q_0}{r} \exp\left(-\frac{r}{\lambda_D} \right), \tag{1.4}$$

which is known as the Debye-Hückel potential and

$$\lambda_D \equiv \left(\frac{\epsilon_0 k_B T_e}{n_i e^2} \right)^{1/2} \tag{1.5}$$

is the Debye length [Bellan, 2006]. In numerical modeling, the particle-in-cell (PIC) resolution should be comparable or less than the local Debye length [Thiebault et al., 2013].

In effect, q_0 generates a classical Coulomb potential at a field point at $r \ll \lambda_D$ while at $r \gg \lambda_D$, q_0 produces an exponentially vanishing potential. Quasi-neutrality only pertains to the latter regime (i.e. $r \sim 5 - 7\lambda_D$) where the potential of q_0 departs from that in a vacuum. The long-range truncation of the electrostatic potential of q_0 in a plasma is known as Debye shielding [Gurnett and Bhattacharjee, 2005]. Debye shielding is an important concept in sheath structures surrounding charged conductors in plasmas.

A negatively charged conducting surface entails a departure from quasi-neutrality in the local ambient plasma; a net electron deficit occurs in the immediate vicinity of the surface generating an ion dominant region of negative plasma potential [Riemann, 1990]. The electron density is insignificant here and regains background levels beyond $n\lambda_D$, that is, beyond the Debye sheath, where quasi-neutrality holds (i.e. $\phi_p \to 0$ and $n_e = n_i = n_0$). The electron and ion distribution profile as a function of distance from a charged surface is

illustrated in Figure 1.1.

In general, the electrostatic influence of a charged conductor on the angular momentum of charged particles dominates when the dimension of the conductor, ℓ, is less than or comparable to $n\lambda_D$ where $n \sim 5 - 7$. This type of interaction is characterized by orbital motion limited (OML) theory and constitutes the thick-sheath model. When $\ell > n\lambda_D$, particle angular momenta is relatively unchanged in what constitutes the space charge regime or thin-sheath model [Samir et al., 1986]. The OML regime is adequately employed for CubeSats of side length ℓ less than or comparable to $n\lambda_D$ [Lai, 2011b], [Whipple, 1981].
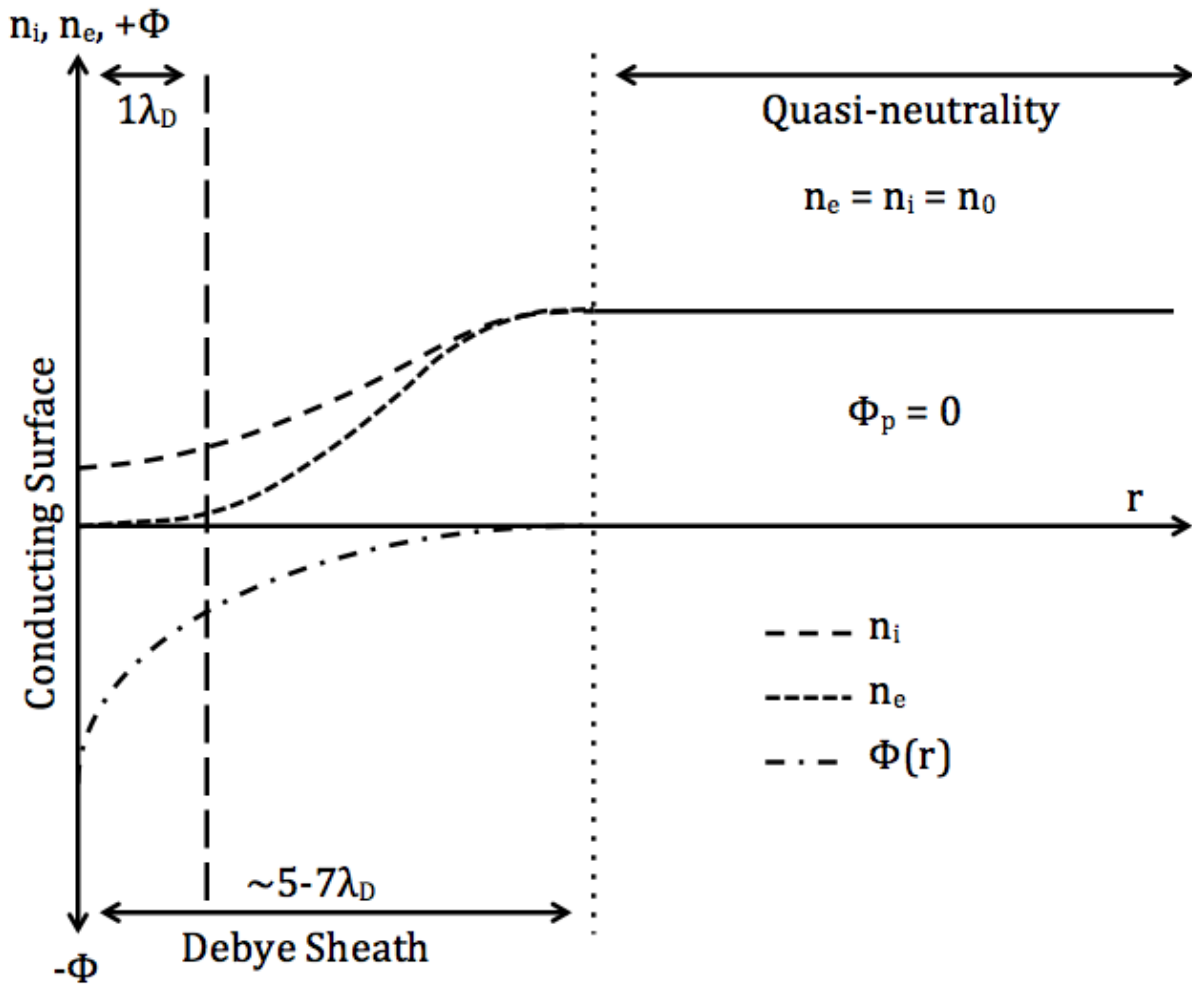
Figure 1.1: The Debye sheath extends $n\lambda_D$ (for $n \sim 5 - 7$) from the negatively charged conducting surface. Within this region, the plasma is non-neutral and $\phi(r) < 0$ for $\phi_f < 0$. Beyond $n\lambda_D$ quasi-neutrality holds where $n_e = n_i = n_0$ and $\phi_p = 0$ (not to scale). Adapted from [Barjatya, 2007].

1.1 Langmuir Probes & Current Balance

A powerful tool in space plasma diagnoses is the Langmuir probe. Langmuir probes apply a known bias voltage, ϕ_b, to a conducting surface and measure the resulting current. The I-V curve (i.e. the collected current as a function of ϕ_b) can be used to determine plasma density and temperatures as well as spacecraft charging [Chen, 1965]. Sounding rockets and satellites typically deploy Langmuir probes into the plasma environment and use theoretical foundations of electrostatic probe theory as developed by Irving Langmuir and Mott-Smith in the mid-1920s to diagnose space plasmas [Langmuir, 1913], [Mott-Smith and Langmuir, 1926]. The important characteristics and features of an I-V curve are shown in Figure 1.2.

In the thick-sheath approximation, the collected electron current density, j, of an arbitrarily shaped Langmuir probe traveling at a speed much less than the thermal velocity of a Maxwellian electron population has a unique form to describe the electron retardation region– the region where ϕ_b resides between the spacecraft potential, ϕ_f, and the ambient plasma potential, ϕ_p, (i.e. $\phi_f < \phi_b < \phi_p$):

$$j_{er} = en_e \left(\frac{k_B T_e}{2\pi m_e} \right)^{1/2} \exp\left(-\frac{e|\phi_b - \phi_p|}{k_B T_e} \right), \tag{1.6}$$

where $|\phi_b - \phi_p|$ is sometimes known as the retarding potential [Brace, 1998]. It is noted that potentials are traditionally considered relative to the plasma potential ($\phi_p = 0$).
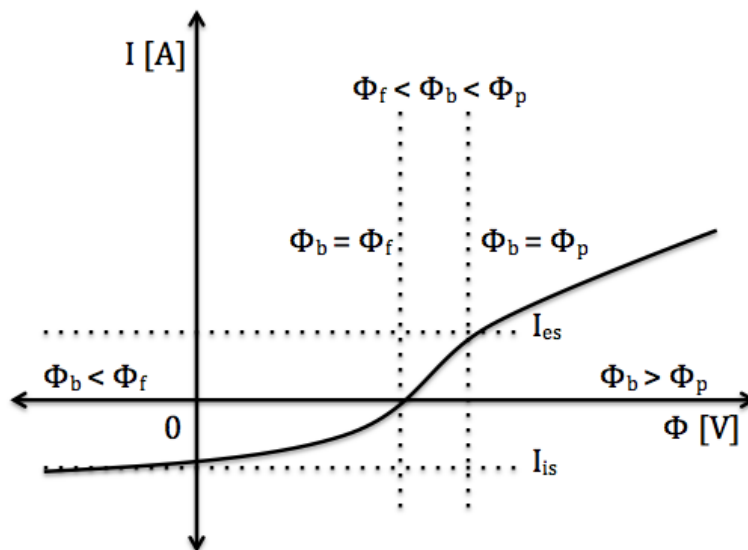
Figure 1.2: The floating potential, ϕ_f, is that where the Langmuir probe collected current is zero. The ion saturation region is where $\phi_b < \phi_f$, the electron retardation region is where $\phi_f < \phi_b < \phi_p$ and the electron saturation region is where $\phi_b > \phi_p$.

When considering the positively charged ion current density, j_i, and all other spurious current densities, j_s, attributable to photoelectrons, secondary and backscattered electrons, etc., the electron retardation region total electron current density may be recast accordingly:

$$j_{er} = en_e \left(\frac{k_B T_e}{2\pi m_e} \right)^{1/2} \exp \left(-\frac{e|\phi_b - \phi_p|}{k_B T_e} \right) - j_i - j_s. \tag{1.7}$$

In tenuous top-side ionospheric plasmas, j_i and j_s may become significant such that gridded Langmuir probes called retarding potential analyzers (RPAs) may be operated to eliminate these currents [Lai, 2012].

The electron number density in the surrounding plasma also pertains to the region beyond ϕ_p (i.e. $\phi_b \gg \phi_p$) known as the electron accelerating or electron saturation region. For probe dimensions comparable to λ_D, the electron current density, j_{es}, collected by a Langmuir probe operating in the electron saturation region may yield an electron number density from a fixed, positive probe potential:

$$j_{es} = 2en_e\pi^{-1} \left(\frac{k_B T_e}{2m_e} \right)^{1/2} \left(1 + \frac{e|\phi_b - \phi_p|}{k_B T_e} \right)^{\alpha}, \tag{1.8}$$

where $\alpha = 1$ for a spherical probe, $\alpha = 1/2$ for a cylindrical probe and $\alpha = 1$ for a planar probe [Brace, 1998].

The electron retardation region encodes information pertaining to the mobility, or temperature, of electrons while the electron saturation region inherits information pertaining to the local electron density.

For a Maxwellian plasma, the derivative with respect to ϕ_b of the logarithm of the electron current collected by the probe of surface area A in Equation 1.6 denotes electron temperature linearity:

$$\frac{d}{d\phi_b}[\log(I_{er})] = -\frac{e}{k_B T_e}, \tag{1.9}$$

where $\log(I_{er}) = -\frac{e}{k_B T_e}|\phi_b - \phi_p| + \log(I_{0re})$, $I_{0re} = en_e A \left(\frac{k_B T_e}{2\pi m_e} \right)^{1/2}$ and $j = IA^{-1}$. The above may be used to compute the electron temperature of the plasma [Chen, 1965].

A negatively biased Langmuir probe will attract ions and repel electrons such that an ion saturation current, $I_{is} = A j_{is}$, is collected. For comparable electron and ion temperatures, the ion saturation current density is described by the the region where $\phi_b \ll \phi_f$:

$$j_{is} = en_i v_i \pi^{-1} \left(1 + \frac{k_B T_i}{m_i v_i^2} + \frac{2e\phi_f}{m_i v_i^2} \right)^{1/2}, \tag{1.10}$$

where v_i is the ion bulk flow velocity [Chen, 1965]. It is apparent from Equation 1.10 that $j_{is} \propto n_i$ such that the ion density may be deduced. In the ionosphere, there is a ram current that exists which is comparable to the ion saturation current.

An s specie current accumulated on the surface of a Langmuir probe of arbitrary geometry, $I_s = I_s(\phi_f)$, is primarily dependent on the particle's velocity at the minimum distance from the probe before electrostatic deflection, called the impact distance, h [Lai, 2012]. More importantly, the orbit-limited Langmuir equation, first derived by Mott-Smith and Langmuir, is

$$I_s(\phi_f) = I_s(0)\eta \left[1 - \frac{q_s\phi_f}{k_B T_s}\right]^\alpha, \tag{1.11}$$

where $I_e(\phi_f)$ $(I_i(\phi_f))$ is the electron (positively charged ion) current collected by a positive (negative) floating potential such that $-\frac{q_s\phi_f}{k_B T_s} > 0$ and $\eta \approx 1.1$ [Mott-Smith and Langmuir, 1926].

The current balance equation expressing the net current collected by a planar conducting surface is one-dimensional and free from effects of particle angular momenta (and thus of particle kinetic energy):

$$I_i(0) - I_e(0) \exp\left(\frac{-q_e\phi_f}{k_B T_e}\right) = 0, \tag{1.12}$$

where $I_s(0) = I_s(\phi_f = 0)\ \forall\ s = i,\ e$ [Lai, 2012].

A Maxwellian velocity distribution, $f_s(\varepsilon)$, in terms of energy, $\varepsilon = \frac{1}{2}m_s\mathbf{v_s}^2$, of an s specie particle with speed v_s repelled by a Langmuir probe of like-sign floating potential will incur a shift in energy equal to the electrostatic potential energy, $q_s\phi_f$, experienced by the particles near the probe. As a result, $f_s(\varepsilon)$ is suitable far from the detector while a shifted Maxwellian velocity distribution, $f_s(\varepsilon + q_s\phi_f)$, describes particle repulsion within the Debye sheath.

The incoming flux of repelled particles on a charged surface in terms of the shifted Maxwellian velocity distribution is

$$\mathbf{\Gamma}_s(\phi_f) = \int_{-\infty}^{\infty} \mathbf{v} f_s(\varepsilon) \exp\left(-\frac{q_s\phi_f}{k_B T_s}\right) d^3v. \tag{1.13}$$

For either $\mathbf{\Gamma}_s(\phi_f) = \mathbf{\Gamma}_i(\phi_f)$ for $q_i > 0$ and $\phi_f > 0$ or $\mathbf{\Gamma}_s(\phi_f) = \mathbf{\Gamma}_e(\phi_f)$ for $q_e < 0$ and $\phi_f < 0$, $f_s(\varepsilon)$ is shifted by an electrostatic potential energy, $q_s\phi_f > 0$, such that the incoming flux of repelled particles exponentially decreases with proximity to the probe [Lai, 2012].

The magnitude of the current generated by repelled s specie particles collected on a surface of like-sign floating potential and surface area A is given by the product of Equation

1.13 and A:

$$I_s(\phi_f) = I_s(0) \exp\left(-\frac{q_s\phi_f}{k_B T_s}\right),$$ (1.14)

where $I_s(\phi_f) = \Gamma(\phi_f)A$, $I_s(0) = \Gamma(0)A$, and $\Gamma(0) = \int_{-\infty}^{\infty} \mathbf{v} f_s(\varepsilon)\, d^3v$. The exponential term in the above is known as Boltzmann's repulsion factor and holds for planar and three-dimensional Langmuir probes [Lai, 2012].

The current balance equation for orbit-limited, attracted and repelled currents on a charged and conducting surface is thus

$$I(\phi_f) = I_s(0)\eta \left[1 - \frac{q_s\phi_f}{k_B T_s}\right]^{\alpha} - I_{r\neq s}(0) \exp\left[-\frac{q_{r\neq s}\phi_f}{k_B T_{r\neq s}}\right],$$ (1.15)

where the first term describes the current collected of attracted species s particles (where $q_s\phi_f < 0$) and the second term denotes the current collected of repelled species $r \neq s$ particles (where $q_{r\neq s}\phi_f > 0$).

It is noted that in Equation 1.15, $\pm q_s = \mp q_{r\neq s}$ for singly-ionized particles given that $k_B T_{r\neq s} \gg q_{r\neq s}\phi_f$ such that $\frac{q_{r\neq s}\phi_f}{k_B T_{r\neq s}} < 1$ (i.e. the repelled species have sufficient thermal energy to overcome the floating potential barrier). Equation 1.15 may be employed to solve for the floating potential for known surface currents [Lai, 2012].

1.2 Spacecraft Plasma Wakes

Similar to the way applied probe potentials determine collected currents on the surface of a Langmuir probe, the potential of a spacecraft is a response from accumulated surface currents [Lai, 2012]. Assuming electrons and ions have the same kinetic energy, electrons are more mobile than the heavier ions. As a result, the thermal electron current on a spacecraft surface exceeds the thermal ion current and the spacecraft charges to a negative potential in the absence of spurious currents. After a given relaxation period, the spacecraft attains an equilibrium potential– a floating potential, ϕ_f– at a zero net collected current. When a spacecraft potential is ϕ_f, it is said to be charged [Chen, 2003].

In worst case scenarios, unmitigated spacecraft charging may compromise an instrument or mission [Gunn and Patel, 2014]. The presence of charged spacecraft disturbs the original state of the plasma environment– in-situ measurements of ambient densities and energies are affected by sheath effects of Langmuir probes [Séran et al., 2005]. Furthermore, the relative velocity of a spacecraft with respect to the plasma generates a spacecraft plasma wake

[Mitharwal, 2011], [Guio and Pécseli, 2005]. PIC codes are commonly employed to simulate plasma wakes for various conditions [Guio and Pécseli, 2005], [Kimura and Nakagawa, 2008], [Birdsall and Langdon, 2004], [Miloch et al., 2008a]. In general, plasma wakes have been seen to be generated by various objects in the space plasma environment: from high velocity dust grains [Melandsø and Goree, 1995], [Maiorov et al., 2000], [Guio and Pécseli, 2005] to planetary bodies [Kimura and Nakagawa, 2008], [Schweigert et al., 1996], [Ogilvie et al., 1996], [Bale et al., 1997], [Farrell et al., 1998].

The rudimentary structure of the spacecraft wake is best expressed in terms of the s specie particle thermal velocity, v_{ths}. The thermal velocity in two-dimensions for an s specie particle is given by

$$v_{ths} \equiv \left(\frac{2k_B T_s}{m_s} \right)^{1/2}.$$
(1.16)

For simplicity, γ_s is defined here as the ratio of an s specie particle thermal speed to the bulk plasma flow velocity which is, effectively, the spacecraft velocity, v_{SC}:

$$\gamma_s = \frac{v_{ths}}{v_{SC}}.$$
(1.17)

The ion flux current density, j_i, on the ram-side surface for $s = i$ and $v_{thi} \ll v_{SC}$ is given by

$$j_i = q_i n_i v_i,$$
(1.18)

where $j_i = I_i A_{ram}^{-1}$, I_i is the ion current collected on the ram-side surface of area A_{ram} and $v_i \approx v_{SC}$ is the incoming ion velocity magnitude [Lai, 2012]. Typical ionospheric plasmas have values of $\gamma_i < 1$ and $\gamma_e > 1$ such that $v_{thi} \ll v_{SC}$ and $v_{the} \gg v_{SC}$, respectively. When $v_{thi} \ll v_{SC} \ll v_{the}$ it is said that meso-thermal conditions apply. Accordingly, electrons are supersonic with respect to the spacecraft– electrons totally engulf the satellite and spacecraft surfaces tend to charge to negative potentials in the absence of spurious currents. Positively charged ions are subsonic with respect to the bulk flow velocity such that they contribute to the ram-side flux current [Lai, 2012]. In this theses, meso-thermal conditions are considered for ionospheric plasmas such that the electron current generated on a CubeSat surface is thermal (i.e. $\gamma_e > 1$) and the ion current is the ion ram current (i.e. $\gamma_i < 1$).

Spacecraft traveling at a velocity v_{SC} in the ionosphere populated by subsonic ions with respect to the spacecraft will produce an ion density depletion immediately downstream the spacecraft [Henderson and Samir, 1967] [Friedrich et al., 2013]. Here, electron thermal

velocities, v_{the}, vastly exceed the bulk velocity of the plasma such that electrons travel upstream and accumulate on wake-side surfaces. As as result, the spacecraft is effectively immersed in negative charge for meso-thermal conditions. In fact, electrons are heated around spacecraft in both the ram-side and wake-side [Siskind et al., 1984], [Singh et al., 1987].

Figure 1.3 shows the traditional view of the meso-thermal plasma wake generated by a negatively charged spacecraft. The uncharged spacecraft will have $n_e = n_0$ and $n_i < n_0$ in the near and far-wake alike; the negatively charged spacecraft has $n_e < n_0$ in the near-wake by electrostatic repulsion and $n_e = n_0$ in the far-wake. It may be easily seen that density measurements differ if a Langmuir probe resides within or outside of a plasma wake; Samir et al. [1987] have shown that there is an asymmetry in the wake current distribution. For spin-modulated Langmuir probe measurements, as those with DICE, the lesser density at any given time corresponds to the probe in the wake while the greater density is thought to be given by the probe outside the wake.
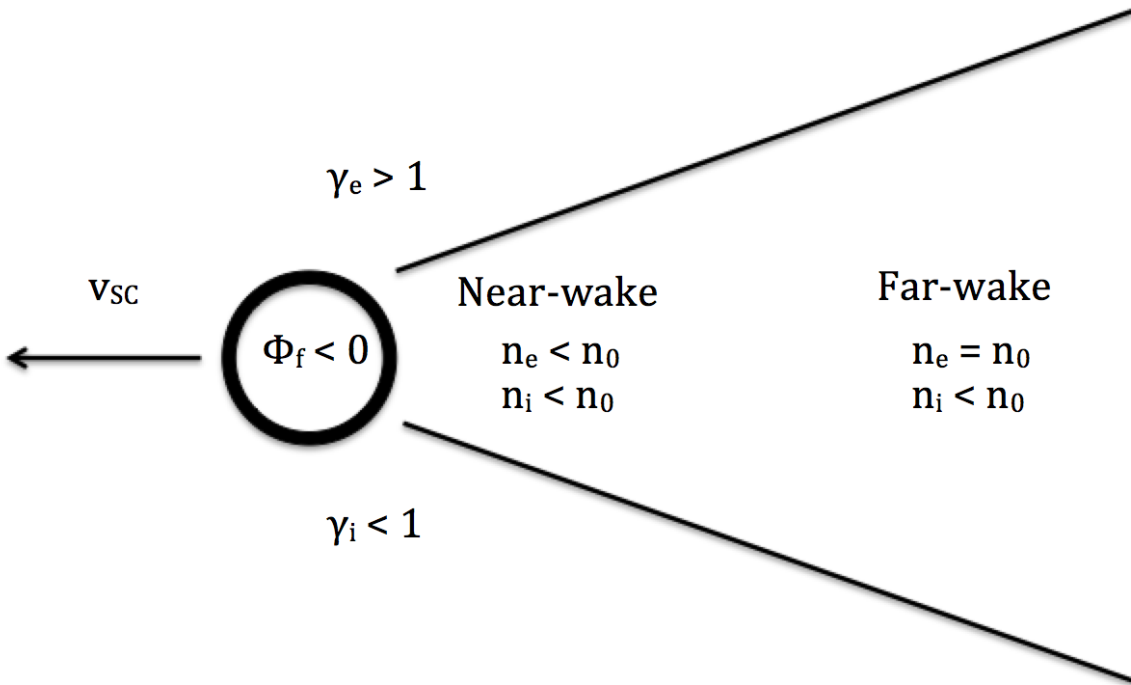
Figure 1.3: The traditional view of the spacecraft plasma wake in the ionosphere (not to scale). Ions generate an ion density depletion in the near and far-wake for meso-thermal conditions.

1.2.1   Ion Focus Region

It has been numerically verified that positively charged ion trajectories may be modulated in the presence of a negatively charged object giving rise to an ion density enhancement in the wake [Vladimirov et al., 2001], [Miloch et al., 2008a]. Heavy ions contribute to the geometric wake structure while the negatively charged conductor acts as an electrostatic lens for light ions [Miloch et al., 2012b]. The region of light ion focusing has been come to be known as the ion focus region [Schweigert et al., 1996].

The ion focus region is dependent on the geometry of the negatively charged body– a degree of asymmetry in focusing is present for elongated objects [Block et al., 2012]. Density enhancements in the focus region are more prevalent for slow ions as cold ions lack the energy to escape the focus region [Miloch et al., 2008a]. The location of maximum enhancement in the focus region resides further downstream for high velocity spacecraft [Miloch et al., 2012b]. Moreover, a potential maximum follows the ion enhancement downstream as given by Poisson's equation [Lampe et al., 2005].
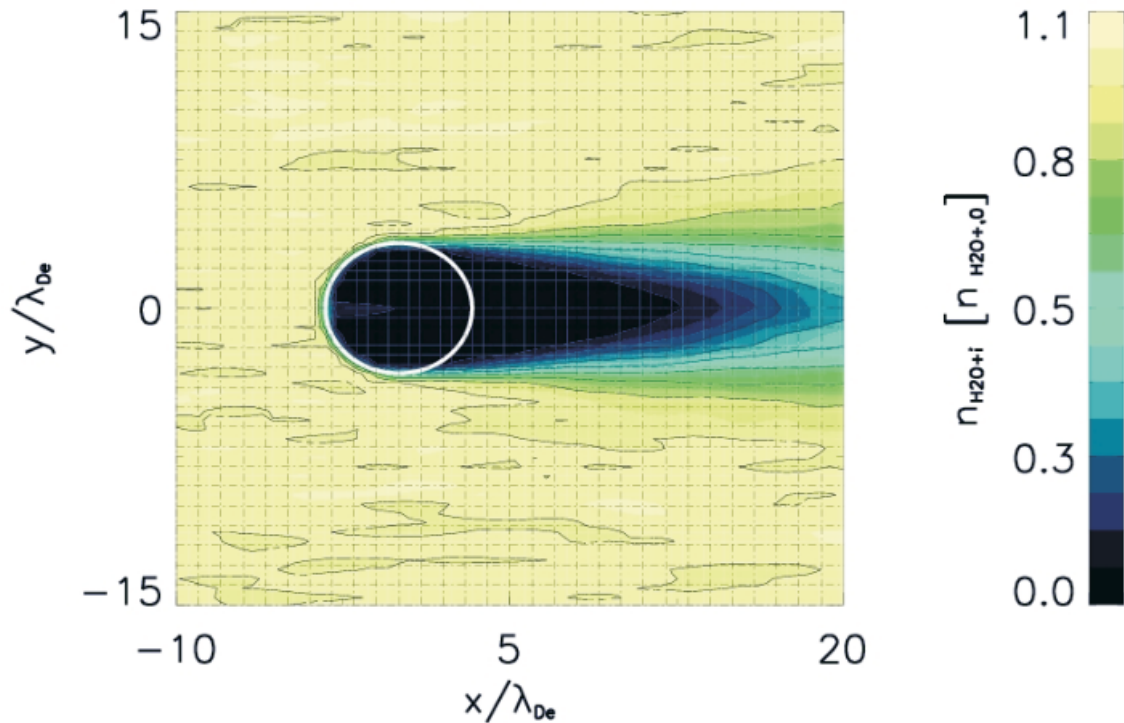
Figure 1.4: The Cassini spacecraft geometric plasma wake generated by heavy water vapor ions within a tenuous plasma of the Saturnian system [Miloch et al., 2012b].

An example of an ion focus region is that simulated by a PIC code simulating the Cassini spacecraft as a simple sphere in a tenuous plasma ($n_0 \approx 5 \times 10^7$ m^{-3}) about four Saturn-radii from Saturn as seen in Figures 1.4 and 1.5. The multi-species Cassini plasma wake consists of a geometric wake generated by heavy water vapor ions and an ion focus region generated by much lighter protons.

The geometric wake shows a density depletion of about $70 - 100\%$ below background that extends about $10\lambda_D$ immediately downstream. In contrast, the ion focus region is seen to begin about $5\lambda_D$ downstream and extend for about $10\lambda_D$ with an enhancement of up to 250% over background.

The ion focus region has also been studied quite extensively for electrically charged dust grains [Melandsø and Goree, 1995], [Maiorov et al., 2000]. More relevantly, ion focusing has been seen in planetary environments [Kimura and Nakagawa, 2008], [Ogilvie et al., 1996]. Nevertheless, previous studies of CubeSat plasma wakes have not denoted ion focusing [Miloch et al., 2012a], [Mitharwal, 2011].
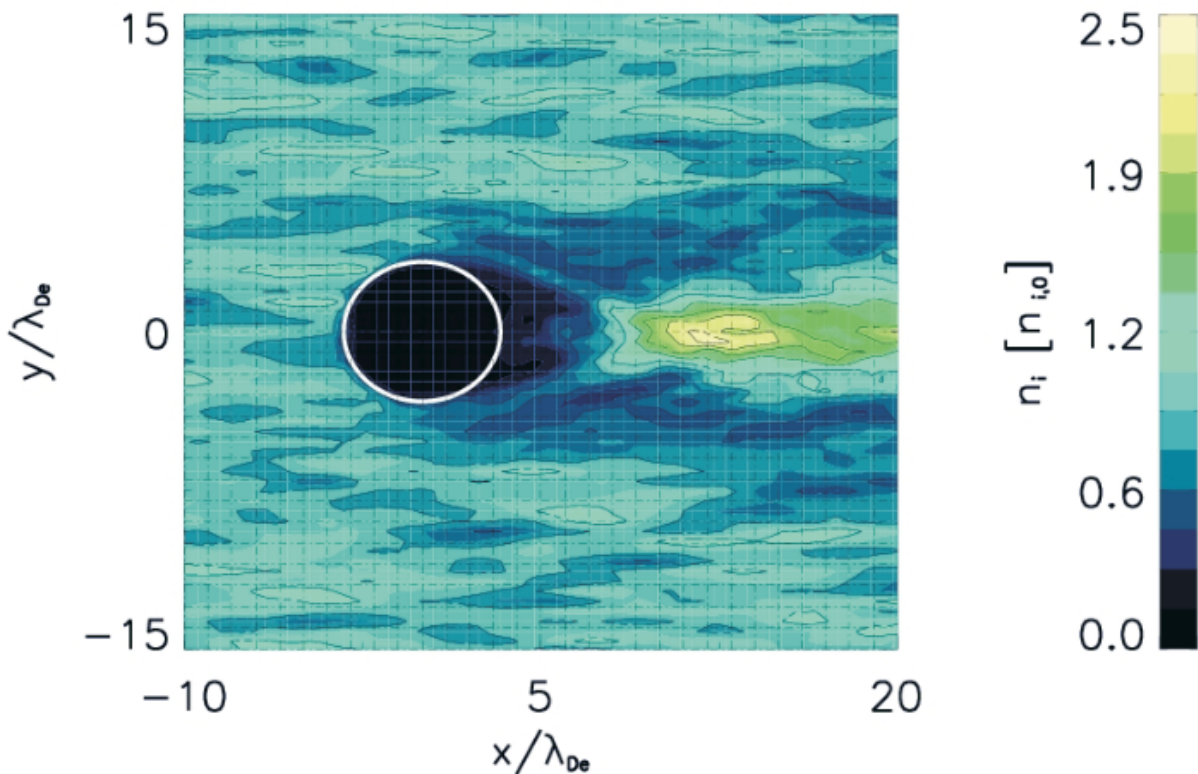
Figure 1.5: The Cassini spacecraft plasma wake with an ion focus region of light ions in a tenuous plasma of the Saturnian system [Miloch et al., 2012b].

1.3 Dynamic Ionosphere CubeSat Experiment

In 1999, Puig-Suari and Twiggs developed a concept of a lightweight and low-cost class of nano-satellite called CubeSat [David, 2004], [Helvajian, 2008]. What began as a 10 cm × 10 cm × 10 cm (1U) CubeSat, has broadened in form up to 12U to satisfy an increasing demand of space science, defense and communications missions by government, industry and academia. The compact nature of CubeSats has deemed this class of spacecraft viable for tandem operations by constellations of multiple CubeSats. Today, clusters of CubeSats developed by international collaborations are deployed with distinct objectives into the space environment. In the CubeSat revolution, the Dynamic Ionosphere CubeSat Experiment (DICE) became the first CubeSat mission designed specifically for scientific operations.

1.3.1 Introduction

Figure 1.6: The two identical 1.5U DICE CubeSats, Farkle (DICE-F) and Yatzee (DICE-Y) [Fish et al., 2012].

DICE consisted of two CubeSats designed in an uncommon 1.5U form factor (i.e. 10 cm ×
10 cm × 15 cm) known as Farkle (DICE-F) and Yatzee (DICE-Y) (shown in Figure 1.6)
[Fish et al., 2012]. The National Science Foundation (NSF) CubeSat and NASA Educational
Launch of Nano-satellites (ELaNa) programs funded the realization of DICE. On October
28, 2011, a Delta II rocket launched DICE from Vandenberg Air Force Base in part of the
NASA ELaNa 3 mission. Deployed simultaneously by NASA's P-POD orbital deployer, the
twin spinning CubeSats assumed a high-inclination ($i = 101.72°$), ~ 97.35 min period orbit
within a ≈ 808 km apogee and ≈ 456 km perigee [Stromberg, 2011].

   Within the first six months, the spacecraft were set to reside within about 300 km of each
other in a "pearls-on-a-string" configuration for temporal-spatial deconvolution of ionospheric
structures. DICE were designed to last for approximately $18,250$ orbits until they de-orbited
by orbital decay at the end of 2014 [Crowley et al., 2011].

1.3.2   Instrumentation

DICE became the first CubeSat cluster specifically funded and designed for science. Instru-
mentation payloads were identical for both DICE-F and DICE-Y and included two fixed-
bias DC Langmuir probes (DCPs), electric field probes (EFPs) and a magnetometer [Crowley
et al., 2011], [Fish et al., 2014]. DC Langmuir and electric field probes were set at a cadence of
0.5 to 1 s corresponding to the ~ 7 to 14 s DICE transit through a so-called storm-enhanced
density (SED) in the ionosphere [Fish et al., 2014], [Stromberg, 2011].

   Two EFP booms were designed to extend 0.5 cm diameter gold-plated spheres 5 m from
each CubeSat perpendicular to two 0.9 m ultra high frequency (UHF) communication booms.
The EFPs were also designed to have a resolution of 100 $\mu V \cdot m^{-1}$ within ± 1 V $\cdot m^{-1}$. This
would be to measure electric fields in the low density plasma wake which are on the order
of ≈ 0.5 mV $\cdot m^{-1}$ [Fish et al., 2012]. Ultimately, the EFP booms were never deployed.

   Two electrically insulated scissor booms held gold-plated, 1 cm diameter spherical Lang-
muir probes (DCPs) 13 cm away from each CubeSat along the 15 cm dimension. This is
seen in Figure 1.7. One DCP, called DCA, was to be held in the ram-side with the second,
DCB, was to be held in the wake-side such that they are aligned with the spin axis and
velocity vector [Fish et al., 2012]. The DCPs were designed to measure ion densities from
2×10^9 m^{-3} to 2×10^{13} m^{-3} at a $\leq 3 \times 10^8$ m^{-3} resolution. The probes operated in the
ion saturation regime with a bias potential of $\phi_b = -4$ V such that ions were collected and
densities were extracted [Stromberg, 2011].
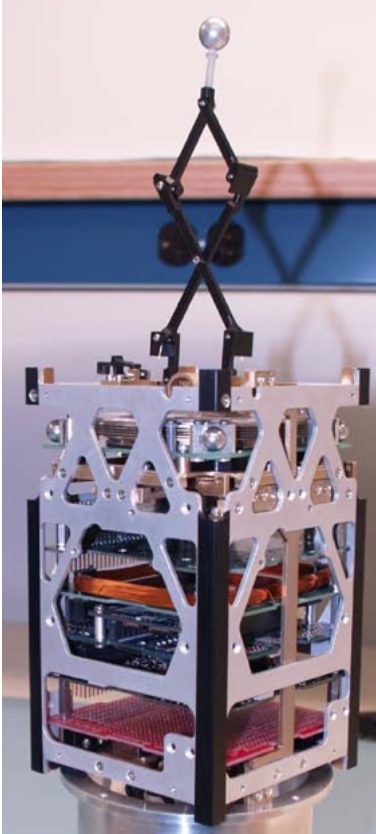
Figure 1.7: A DICE CubeSat with a fully extended Langmuir probe [Fish et al., 2014].
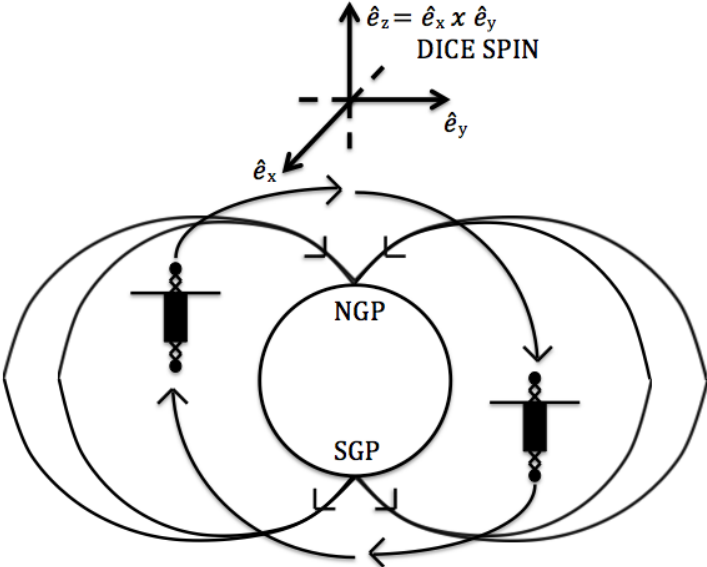
Figure 1.8: DICE orbit and spin about the $\hat{e}_z$ axis. DCP positions were supposed to be held in the wake and ram directions with EFP boom orthogonal to magnetic field lines. The attitude of DICE was never solved.

Spacecraft spin axes were set to reside within 1σ ($\leq 5°$) of the epoch J2000 inertial z-axis throughout each orbit [Fish et al., 2014]. The attempted satellite attitude would allow for plasma density and electric potential data acquisition by DCPs in the spacecraft ram and wake directions at any given time. However, since DICE were tumbling without control, density measurements by the DCPs are spin-modulated.

1.4 Spacecraft Plasma Interaction System

An integral component of spacecraft design is the ability to assess the worst case scenario for spacecraft charging. Mostly used for geosynchronous (GEO) orbits, spacecraft charging codes have been employed for various spacecraft geometries to numerically compute surface currents and electric potentials on surfaces and in the surrounding plasma. For nearly 20 years, NASA Charging Analyzer Program (NASCAP) has dominated the spacecraft charging industry [Lai, 2011b]. NASA and commercial entities have developed GEO, low Earth orbit (LEO) and polar Earth orbit (PEO) charging codes such as NASCAP-GEO, NASCAP-LEO and POLAR, respectively.

Today, NASCAP is rivaled by the European Space Agency (ESA) contracted Spacecraft Plasma Interaction System (SPIS). SPIS began in December of 2002 with the SPIS user interface called SPIS-UI (Artenum, Paris) and the SPIS numerical kernel called SPIS-NUM (ONERA).

SPIS was released in March of 2004 as an open-source code written in Python/Jython with a Java graphical user interface (GUI). It is part of the spacecraft-plasma interaction collaborative platform for advanced information exchange called the Spacecraft Plasma Interactions Network in Europe (SPINE). Today, SPIS is the European standard multi-platform numerical code for spacecraft-plasma interactions.

1.4.1 Pre-processing

One advantage of SPIS over other charging codes is its ability to model detailed three-dimensional spacecraft geometries [Lai, 2011b]. Spacecraft models are generated by the boundary representations (B-reps) method of point, line, surface and volume (PLSV) hierarchy within the Computer Assisted Design (CAD) and meshing visualization toolkit called Gmsh [Sookahet, 2003]. Spacecraft and surrounding plasma regions are defined by closed surfaces in Gmsh. A computational volume is delimited by surfaces as seen in Figure 1.9.

Proceeding the meshing of the spacecraft geometry, local parameters are allocated on

disparate spacecraft components. Local parameters are boundary conditions pertinent to spacecraft materials which are deployed onto the meshed groups in the form of DataFields. Spacecraft surface groups are given specific conductivities, temperatures, and properties by the *Groups Editor*. Surface materials may be chosen from a NASCAP-based materials dataset or from an imported dataset. In the *Groups Editor*, plasma, electric field and meshing conditions may be also be assigned onto the external boundary group.

Proceeding the allocation of DataFields onto spacecraft groups, an internal circuit may be included in the *Electrical Circuit Editor* for electrically isolated nodes. Dynamic charging effects are simulated for each electrical node as they are connected through resistors, capacitors and voltage generators. The SPIS user is granted the ability to advance the spacecraft detail at ease by the user friendly local parameter interface [Thiebault et al., 2013].

Spacecraft properties not deployable onto the geometry may be prescribed alongside ambient plasma parameters and simulation specifications in the *Global Parameters Editor* as seen in Figure 1.10. Attitude information may be accounted for by three-dimensional magnetic flux densities and the Sun's position (with optional photoemission) in the *B Field* and *Surface Interactions* tabs of the *Global Parameters Editor*, respectively.

The *Plasma* tab allows for spacecraft interactions with a multiple specie plasma as specified by temperatures and densities of two electron and ion populations. The duration and time-steps of the simulation may be set by the *duration* and *simulationDt* parameters in the *Simulation control* tab, respectively.
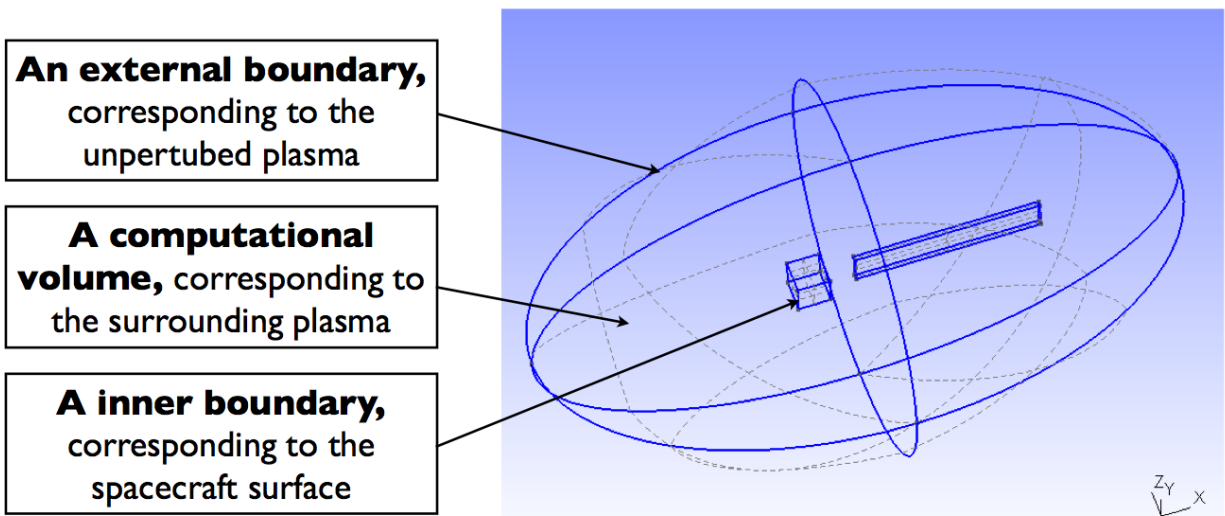
Figure 1.9: Example of spacecraft geometry with surrounding plasma computational volume in Gmsh [Thiebault et al., 2013].

The *Spacecraft* tab allows the inclusion of an initial floating potential, absolute spacecraft capacitance and internal circuit by the *initPot*, *CSat* and *electricCircuitIntegrate* parameters, respectively. Once all global parameters are adequately assigned to reflect ambient space plasma conditions, the *Finalize run configuration and save project* button is pressed to input all local and global parameters into the numerical kernel. This converts fields from the SPIS-GEO to the SPIS-NUM data structure [Thiebault et al., 2013].

Name	Type	Value	Unit	Description	Verbosity
electronDistrib2	String	PICVolDistrib	None	Name of the VolDistrib class to be used for the 2nd...	LOW
ionVx2	double	0.0	[m/s]	Ion drift velocity along x axis (2nd population)	LOW
ionDensity	double	1000000.0	[m−3]	Ion density (1st population)	LOW
ionDistrib	String	PICVolDistrib	None	Name of the VolDistrib class to be used for ions	LOW
ionType2	String	H+	None	Second ion population	LOW
ionType	String	H+	None	First ion population	LOW
ionVz	double	0.0	[m/s]	Ion drift velocity along z axis (1st population)	LOW
electronDt2	double	−1.0	[s]	Maximum integration time step for electron 2nd pop...	LOW
ionDt2	double	−1.0	[s]	Maximum integration time step for ion 2nd populati...	LOW
avPartNbPerCell	double	5.0	None	average number of super−particle per cell	LOW
ionSpeedUp	double	1.0	[−]	Numerical times speed−up factor for ion 1st populat...	LOW
environmentType	String	BiMaxwellianEnviro...	None	Name of the Environment class to be used	LOW
electronDensity	double	1000000.0	[m−3]	Electron density (1st population)	LOW
ionDensity2	double	0.0	[#/m3]	Ion density (2nd population)	LOW
ionTemperature	double	1.0	[eV]	Ion temperature (1st population)	LOW
electronTemperature2	double	1000.0	[eV]	Electron temperature(2nd population)	LOW
ionVy	double	0.0	[m/s]	Ion drift velocity along y axis (1st population)	LOW
ionVy2	double	0.0	[m/s]	Ion drift velocity along y axis (2nd population)	LOW
ionVx	double	0.0	[m/s]	Ion drift velocity along x axis (1st population)	LOW
electronDt	double	−1.0	[s]	Maximum integration time step for electron 1st pop...	LOW
electronDensity2	double	0.0	[#/m3]	Electron density (2nd population)	LOW
ionDistrib2	String	PICVolDistrib	None	Name of the VolDistrib class to be used for ions 2nd...	LOW
ionVz2	double	0.0	[m/s]	Ion drift velocity along z axis (2nd population)	LOW
electronDistrib	String	PICVolDistrib	None	Name of the VolDistrib class to be used for electrons	LOW
ionTemperature2	double	1000.0	[eV]	Ion temperature (2nd population)	LOW
ionSpeedUp2	double	1.0	[−]	Numerical times speed−up factor for ion 2nd popul...	LOW
ionDt	double	−1.0	[s]	Maximum integration time step for ion 1st populatio...	LOW
electronTemperature	double	1.0	[eV]	Electron temperature(1st population)	LOW
electronSpeedUp	double	1.0	[−]	Numerical times speed−up factor for electron 1st po...	LOW
electronSpeedUp2	double	1.0	[−]	Numerical times speed−up factor for electron 2nd p...	LOW

Figure 1.10: Assignment of plasma and simulation parameters in preparation of the numerical kernel is done in the *Global Parameters Editor*.

1.4.2   User Interface & Numerical Design

SPIS consists of the SPIS user interface (SPIS-UI) and the SPIS numerical kernel (SPIS-NUM). SPIS-UI was developed from a generic Integrated Modeling Environment (IME) called Keridwen by Artenum, Paris. To optimize SPIS preprocessing, Keridwen employs the Artenum Penelope and Frida libraries for spacecraft meshing, groups and DataFields [Thiebault et al., 2013].

The friendly SPIS-UI GUI is best witnessed by the wizard-based approach. A straightforward pre-processing, solving and post-processing sequence chain is seen in Figure 1.11. The progressive sequence through the modeling chain enables the user to return to previous stages once completed to modify the data model. SPIS-UI automatically saves projects as the user navigates pre and post-processing stages and automatically generates sub-directories within the SPIS root directory.

SPIS-NUM incorporates a finite element method of solving the electrostatic Poisson equation for surface and volume potentials and volume electric fields within a three-dimensional bounded domain [Rogier and Volpert]. Dirichlet, Neumann and Robin conditions are prescribed on conducting surface groups, dielectric surface groups and external boundary groups as auxiliary conditions on the near-spacecraft electrostatic potential, electric field normal component and far-spacecraft electrostatic potential, respectively.

The linear Poisson equation is solved iteratively by a preconditioned conjugate gradient (PCG) algorithm. The non-linear Poisson formalism, which is stable for PIC cells larger than Debye lengths, is solved via Newton's method through the linear Poisson PCG algorithm solution [Rogier and Volpert]. The *Poisson equation* tab in the *Global Parameters Editor* allows for the specification of a linear or non-linear Poisson solver (by the *linearPoisson* flag).
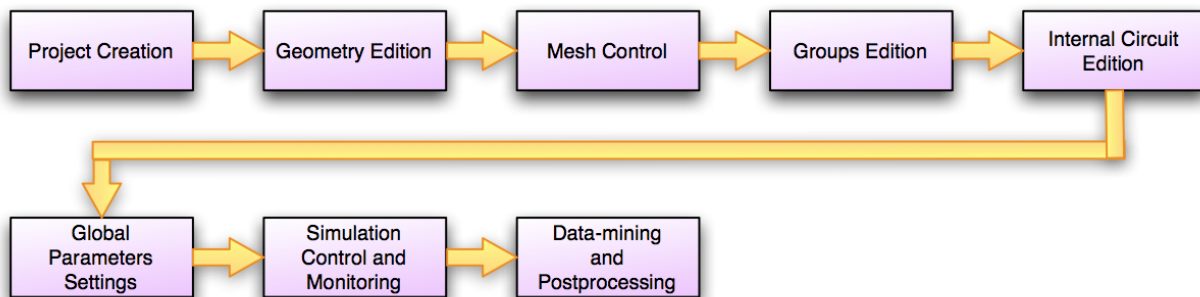
Figure 1.11: The SPIS-UI logical sequence from CAD creation and preprocessing to data-mining and post-processing.

Tolerances and maximum iteration numbers of the conjugate gradient Poisson solver are specified by the *tolGradient* and *tolGradientNl* values and *iterGradient* and *iterGradientNl* values for linear and non-linear Poisson solvers, respectively. If the user desires to obtain a non-linear Poisson solution, the maximum iteration and tolerance for convergence of Newton's method, given by the *tolNewton* and *iterNewton* values, must also be considered [Rogier and Volpert], [Thiebault et al., 2013]. PIC modeling may be assigned to biMaxwellian electron and ion distributions in the *Plasma* tab of the *Global Parameters Editor* by assigning the *PICVolDistrib* value. This setting uses Monte Carlo PIC macro-particle motions integrated by a leap-frog scheme while macro-particle densities are interpolated from their positions [Thiebault et al., 2013].

The completion of the pre-processing stage is marked by the conversion of SPIS-UI data into the numerical solver of SPIS-NUM. This is done in the *Simulation Control and Monitoring Panel* of the SPIS numerical kernel where the user may select components in the *Instrument list viewer* to view the progress of virtual instruments as the simulation is running. Virtual instrument output monitoring is seen on the right-hand-side of Figure 1.12 which is updated in real-time [Thiebault et al., 2013]. Once completed, the simulation may be finalized whereby data is extracted for data mining in the post-processing stage or continued by an update of the simulation time.
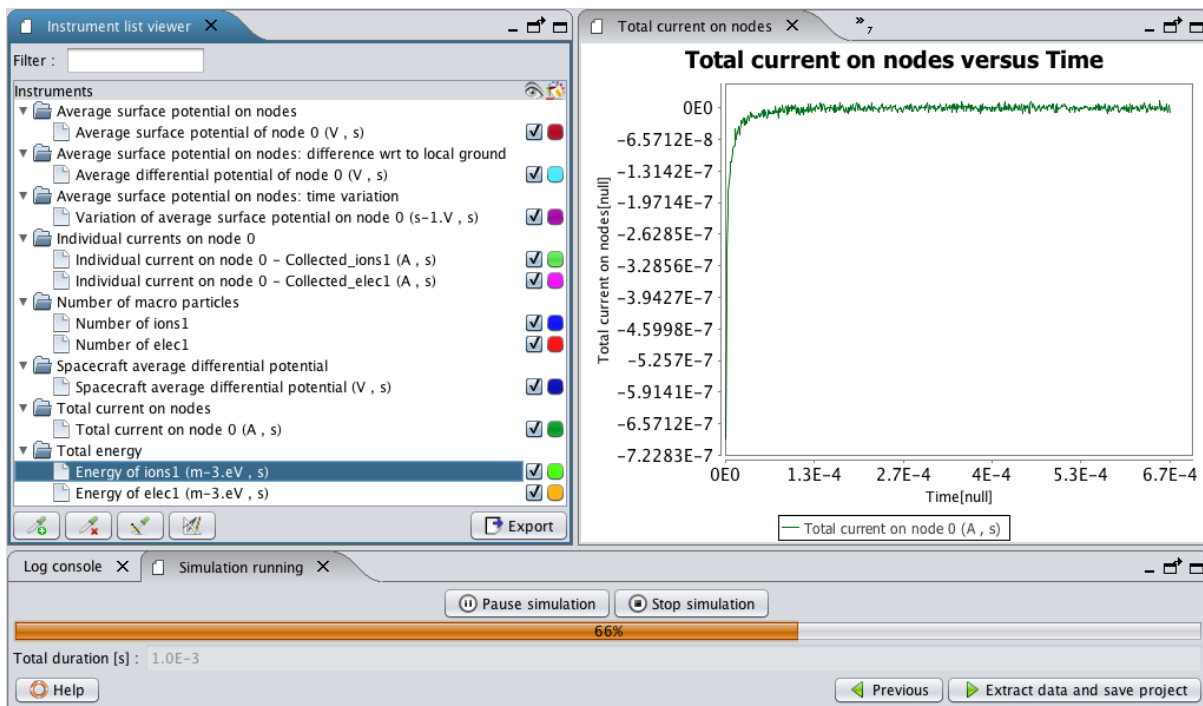
Figure 1.12: The SPIS-NUM solver in action in the *Simulation Control and Monitoring Panel*.

1.4.3   Post-processing

Once a simulation is completed, SPIS-NUM yields a post-processing stage where histograms and two-dimensional and three-dimensional visualizations facilitate data analysis. The *Data Miner* page consists of a post-processing panel on the left-hand-side of the screen and a corresponding rendering panel on the right as seen in Figure 1.13.

   The post-processing panel allows for the facilitated filtering of data to be visualized. The *Distribution Functions* directory allows the visualization of PIC macro-particle distribution histograms of particle populations per geometrical node at different times throughout the simulation. Average floating potential, both differential and surface, and spacecraft surface currents- by geometrical node- time-series may be seen by selecting the desired two-dimensional visualization within the *Time Series* directory of the post-processing panel.

   DataField solutions at nodes, edges and surfaces may be visualized by a generic three-dimensional scientific data viewer called *Cassandra*. Three-dimensional visualization of spacecraft surface currents, electric fields and potentials at sequential simulation intervals may be accessed through the *Surface Collected Currents*, *Surface Electric Fields* and *Surface Potentials* directories of the post-processing panel, respectively. Moreover, Cassandra enables the three-dimensional visualization of electric fields, plasma densities, macro particle number densities and potentials in the computational volume at various times of the simulation.
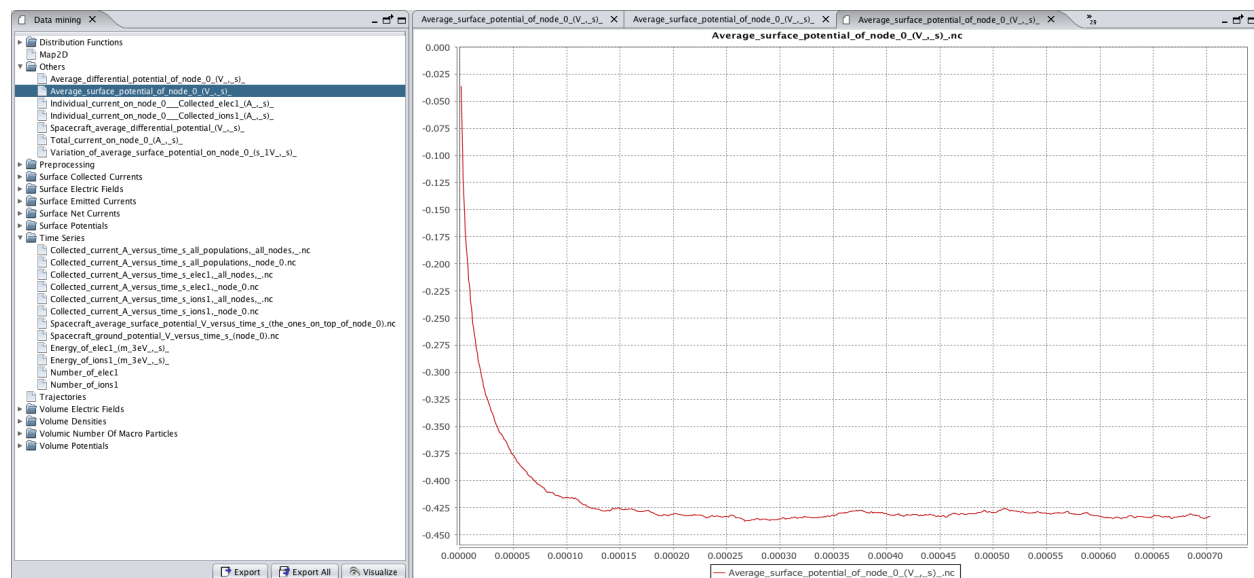
Figure 1.13: The SPIS *Data Miner* page with the post-processing panel and average differential potential as a function of time plot in the rendering panel.

External plugins may be loaded to facilitate and extend the viewing capabilities of Cassandra which may compliment the included three-dimensional filters within the Cassandra *Filters* menu. Some of the filters within SPIS include the *Glyph* filter which displays arrows denoting vectors, the *Cutting plane* filter which displays two-dimensional slicing along a specified axis for computational volume cross-sectional analysis and the *Clipping* filter which displays a volumetric slicing along a specified axis in a half-space extraction of the computational volume. Data mining features may be individually or cumulatively visualized in the rendering panel and exported into a directory of choice. When simulations are paused and durations are extended, all previous results are retained under the corresponding project directory.
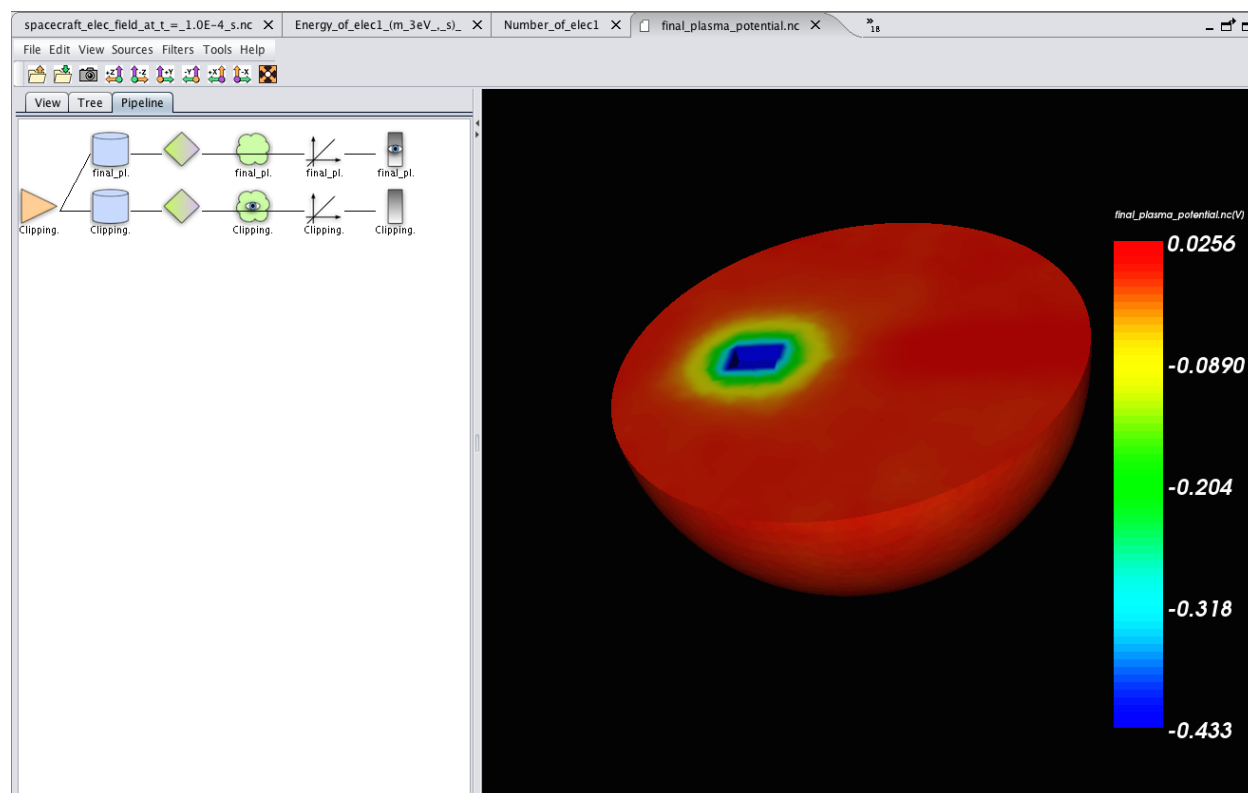
Figure 1.14: The *Clipping* filter in the Cassandra graphical pipeline editor as applied onto a computational volume potential in the rendering panel.

Chapter 2

SURFACE CHARGING OF A STATIONARY CUBESAT

A preliminary investigation into the numerical foundations of SPIS is performed in a cross-sectional analysis of surface charging effects of a DICE CubeSat immersed within a non-flowing plasma. The 1.5U CubeSat is inserted in six distinct plasma conditions. The plasma environments of the CubeSat simulated reflect simplicity: they are non-flowing, non-magnetized, in the absence of solar flux and spurious emissions and consistent with the thick-sheath approximation of Langmuir probes. They consist of one electron population and one ion population of singly ionized oxygen ions.

To avoid unwanted spurious particle accelerations, when running electron PIC populations with the linear Poisson solver, SPIS requires that the product of the plasma dynamic time-step and plasma frequency is less than 0.2 (i.e. $plasmaDt < 0.2\omega_p$). In these conditions, the meshing resolution, res, must be less than λ_D to avoid crude plasma interactions at sub-Debye length scales. These constraints are not required for Maxwell-Boltzmann electron population distributions in the nonlinear Poisson solver. Ion populations, however, are best simulated through PIC since subsonic ion thermal velocities with respect to the spacecraft are not isothermal and may not be modeled with a Maxwellian distribution. Ultimately, the meshing resolution and time-step for plasma dynamics is selected to be on the same order of magnitude as the local Debye length and plasma frequency inverse, respectively.

Abiding by the B-reps geometrical hierarchy in Gmsh, the DICE CubeSat is created and placed in the center of a $r = 0.4$ m radius spherical computational volume such that the CubeSat is totally immersed in the plasma. It is verified that the floating potential, ϕ_f, is independent of plasma density.

Table 2.1: Global parameters of six SPIS simulations of a stationary CubeSat in LEO for charging analysis.

Simulation	n_0 [m^{-3}]	$T_e = T_i$ [K]	$electronDt = ionDt$ [s]	$simulationDt$ [s]
1	1×10^9	1000	5×10^{-6}	2.75×10^{-4}
2	1×10^9	2000	1×10^{-6}	2.75×10^{-4}
3	1×10^9	3000	1×10^{-7}	2.75×10^{-4}
4	1×10^8	1000	1×10^{-5}	5×10^{-3}
5	1×10^8	2000	1×10^{-6}	5×10^{-3}
6	1×10^8	3000	1×10^{-6}	5×10^{-3}

For simplicity, the DICE CubeSat is modeled as a single electrical node with an aluminum surface. The rudimentary and meshed geometry used for the simulation set is illustrated in Figure 2.1. The electron population is modeled as a Maxwellian distribution while the O^+ ion population is simulated as a PIC model such that the non-linear Poisson solver is used. No magnetic fields nor solar fluxes were included in these simulations. Each of the six simulations show current balance and resulting floating potential at a charging time, τ_C, defined as the time of zero net current. The primary plasma properties of each of the simulations are overviewed in Table 2.1. It is noted that for a leading-order approximation of charging dynamics, a plasma time-step of $plasmaDt = 1 \times 10^{-6}$ s is used to be comparable to the inverse of the local plasma frequency on the order of 1×10^6 Hz.
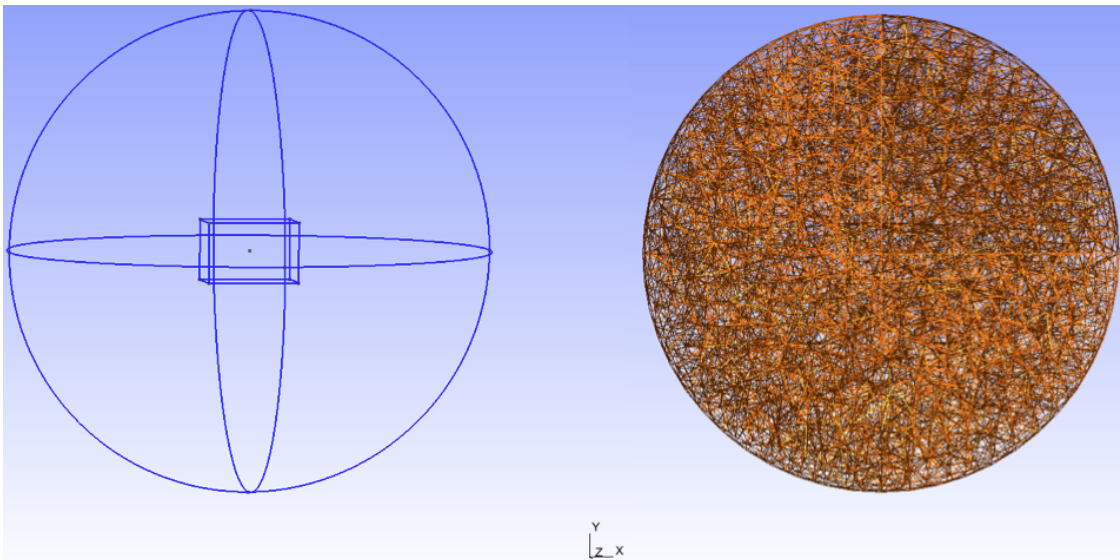
Figure 2.1: Gmsh geometry of the DICE CubeSat centered within a spherical computational volume used for non-flowing SPIS simulations.

2.1   Results & Conclusion

The time-series profiles of the surface potential are categorized by plasma density and shown in Figures 2.2 and 2.3 for $n_0 = 1 \times 10^9$ m^{-3} and $n_0 = 1 \times 10^8$ m^{-3}, respectively, each having $T_e = T_i = 1000$ K, 2000 K and 3000 K temperatures. It is apparent that SPIS denotes higher floating potential magnitudes attained at slightly longer times for a constant plasma density and higher plasma temperatures. Alternatively, higher plasma densities ensure faster surface current balance; the floating potential value is independent of plasma density and has a magnitude directly proportional to electron and ion temperature. This is expected as plasma density terms cancel within the current balance equation. The charging levels and times are tabulated in Table 2.2. In conclusion, higher plasma densities allow for rapid charging of conducting surfaces. Charges in abundance accumulate on surfaces by purely thermal motion and consequently attract opposite charge to achieve current balance.
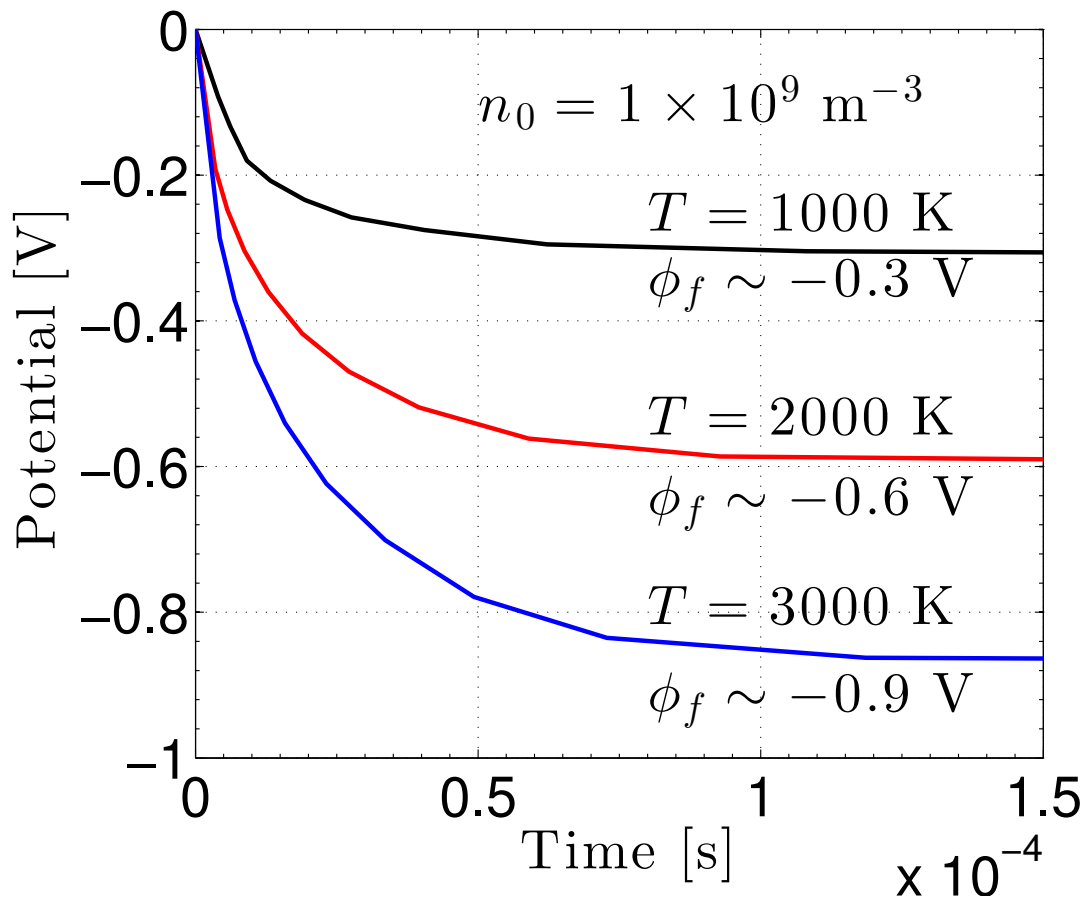
Figure 2.2: SPIS-rendered floating potentials for the stationary DICE-F CubeSat in a 1×10^9 m^{-3} density plasma .

Table 2.2: Charging times and floating potentials for the six SPIS simulations of the stationary CubeSat.

Simulation	n_0 [m^{-3}]	$T_e = T_i$ [K]	τ_C [s]	ϕ_f [V]
1	1×10^9	1000	6.22×10^{-5}	-0.30
2	1×10^9	2000	9.28×10^{-5}	-0.59
3	1×10^9	3000	1.19×10^{-4}	-0.87
4	1×10^8	1000	4.70×10^{-4}	-0.27
5	1×10^8	2000	1.10×10^{-3}	-0.58
6	1×10^8	3000	2.10×10^{-3}	-0.90
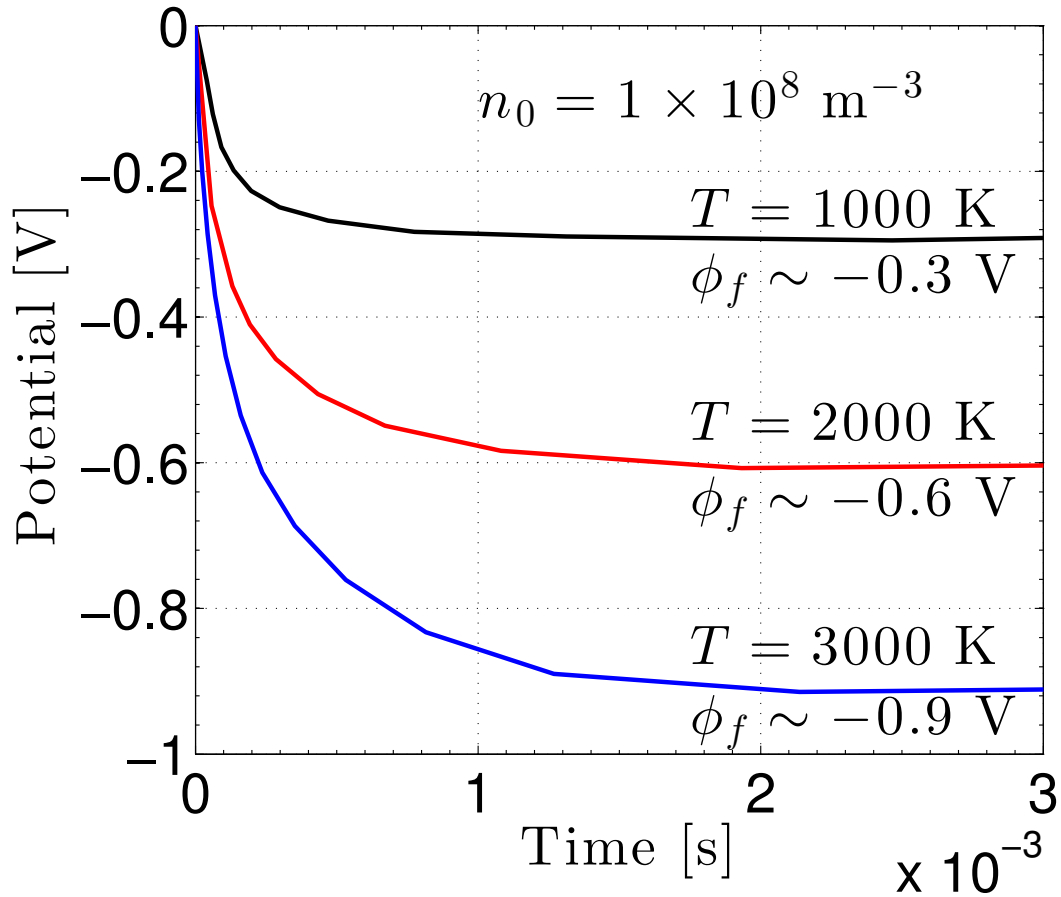
Figure 2.3: SPIS-rendered floating potentials for the stationary DICE-F CubeSat in a 1×10^8 m^{-3} density plasma.

Lower electron and ion temperatures allow for the facilitation of surface charging as charged particles have less energy to penetrate the Coulomb potential barrier set forth by the collection of like charges; high energy particles are more immune to the electrostatic repulsion thus increase the time for potential equilibrium and equivalently for the total surface current to tend to zero. The average floating potential for $T_e = T_i = 1000$ K is $\langle \phi_f \rangle_1 = -0.3$ V, for $T_e = T_i = 2000$ K is $\langle \phi_f \rangle_2 = -0.60$ V and the average floating potential for $T_e = T_i = 3000$ K is $\langle \phi_f \rangle_3 = -0.90$ V.

Spacecraft surface charging simulations with SPIS show a range of charging times, 6.22×10^{-5} s $\leq \tau_C \leq 2.1 \times 10^{-3}$ s for plasma densities of $n_0 = 1 \times 10^8$ m^{-3} and $n_0 = 1 \times 10^9$ m^{-3}, and plasma temperatures 1000 K $\leq T_e = T_i \leq$ 3000 K. These conditions correspond to floating potentials between -0.9 V $\leq \phi_f \leq -0.3$ V. The fastest charging time is for the first simulation, which has the combination of low temperature and high plasma density. Similarly, the slowest charging time is for the last simulation which has the highest electron and ion temperature and lowest density. Accordingly, $(T_e, T_i) \propto \tau_C$ and $n_0 \propto \tau_C^{-1}$. When solving for ϕ_f in Equation 1.15, it is seen that n_0 cancels such that $\phi_f \neq \phi_f(n_0)$. Moreover, the current balance equation states that $|\phi_f| \propto (T_e, T_i)$ and, for non-flowing plasmas, ϕ_f is not a function of collecting surface area, A. These fundamental concepts of surface charging are verified by SPIS results.

Chapter 3

SPIS SIMULATIONS OF THE DICE CUBESAT

The DICE CubeSats began gathering in-situ density measurements upon deployment of the DCA and DCB Langmuir probes. A data sample of DCP detections was selected on May 26, 2012– a relatively quite time in geomagnetic activity. The intended spin axis of DICE was not stabilized and the CubeSats were tumbling uncontrollably. In effect, the probes alternately spin into and out of the wake such that one probe measures a density enhancement relative to the other at any given time. The relative difference in measured density is at a minimum when the spacecraft rotates along the axis perpendicular to the axis of the DCPs. The maximum densities detected in each spin-cycle were normalized to a model generated by the National Oceanic and Atmospheric Administration (NOAA)/Space Environment Corporation (SEC) space weather service called the Ionosphere Forecast Model (IFM). The normalized DCP data varies with density changes in altitude such that it denotes a quasi-periodic oscillation through each ~ 97.35 min orbital period. The spin-modulated data is shown in Figure 3.1.

3.1 Simulation Parameterization

According the International Reference Ionosphere (IRI) model, the plasma density varies from 7.99×10^9 m$^{-3} \leq n_0 \leq 7.93 \times 10^{11}$ m^{-3} between 1.3 hr and 10.5 hr UTC on May 26, 2012. The minimum plasma density during this data sample is at the top-side ionosphere altitude of $z = 811.28$ km where the IRI electron temperature is $T_e = 2395.8$ K and $\lambda_D = 3.8 \times 10^{-2}$ m. The maximum plasma density of during this time is at the F-region altitude

of $z = 496.84$ km where $T_e = 1193.2$ K and $\lambda_D = 2.7 \times 10^{-3}$ m. Within this data sample is a cycle where the DCPs do not resolve relative densities at high altitudes where the density is low. This is seen in Figure 3.1. The spin-modulated density data is best seen in Figure 3.2.

In an attempt to avoid plasma transport effects and complexities towards polar latitudes, a moderate latitude location of DICE-F is selected for investigation. Also, a high altitude, low density location is sought for low computational expense when using PIC. Lastly, a time at night is favorable such that positive charging by photoemission is absent. As a result, the DICE-F location of $\varphi = -69.90°$ latitude, $\lambda = 296.40°$ longitude and $z = 748.16$ km altitude at $t = 2.09$ hr UTC is selected. Here, the IRI-based plasma density is $n_0 = 8.09 \times 10^9$ m^{-3} and the electron temperature is $T_e = 2065$ K such that $\lambda_D = 3.5 \times 10^{-2}$ m. At the time of interest, the detected DCA and DCB plasma densities are $n_{0DCA} = 3.00 \times 10^{10}$ m^{-3} and $n_{0DCB} = 5.98 \times 10^9$ m^{-3}, respectively. The IRI-based ion temperature at this time is $T_i = 1413$ K.
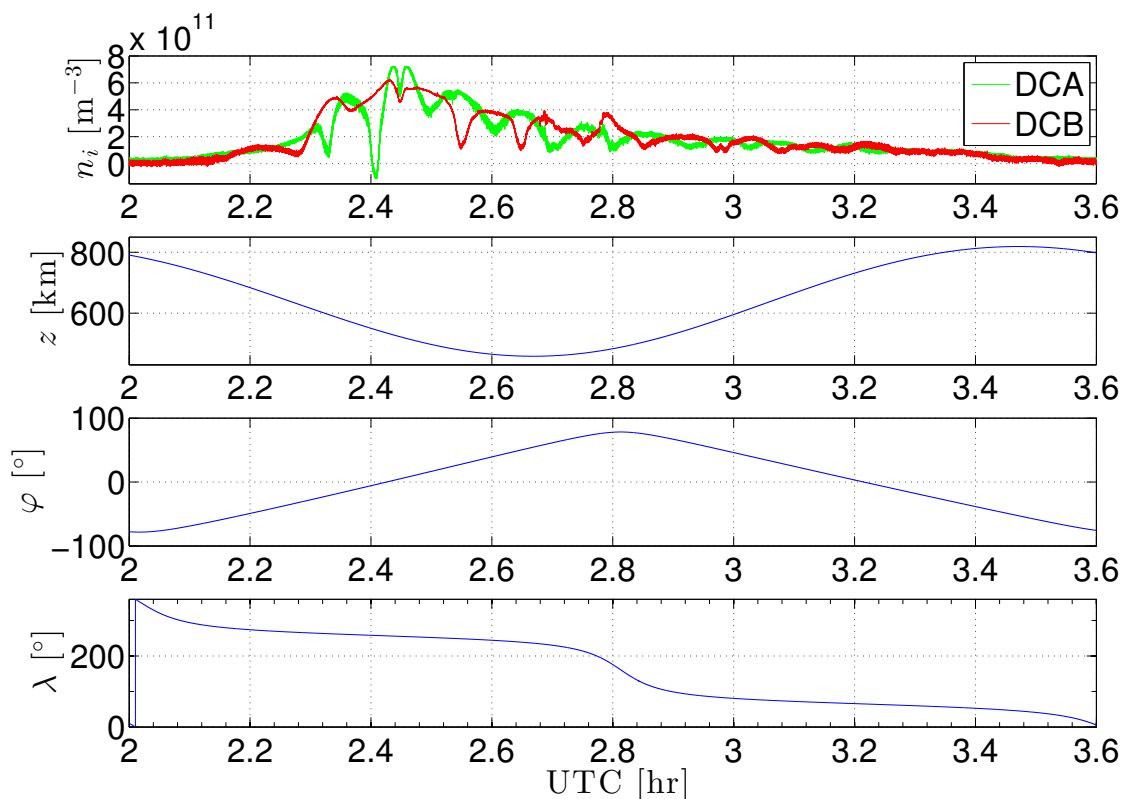
Figure 3.1: The DCA, DCB plasma densities and DICE altitude, latitude and longitude from 2 hr to 3.6 hr UTC on May 26, 2012. The tumbling DICE CubeSat is believed to show ion densities dip and rise as the DCPs enter and exit the wake.

Table 3.1: Parameters of the selected data sample of DICE-F on May 26, 2012.

n_0 [m^{-3}]	8.09×10^9	t [hr, UTC]	2.09
T_e [K]	2065	φ [°]	-69.90
T_i [K]	1413	λ [°]	296.40
v_{the} [m $\cdot$ s^{-1}]	1.77×10^5	z [km]	748.16
v_{thi} [m $\cdot$ s^{-1}]	1.2×10^3	v_{SC} [m $\cdot$ s^{-1}]	7549
ω_p [rad $\cdot$ s^{-1}]	5.07×10^6	λ_D [m]	3.5×10^{-2}
n_{0DCA} [m^{-3}]	3.00×10^{10}	n_{0DCB} [m^{-3}]	5.98×10^9

The temperatures selected are referenced from the ion and electron temperature profiles with altitude as illustrated in Figure 3.3. Figure 3.3 shows that the dominant ion at the altitude of interest is O$^+$. It is noted that temperatures and densities are not extracted from DCP I-V curves in this study such that existing ionospheric models are not refined. Table 3.1 gives pertinent parameters to the DICE-F data sample.
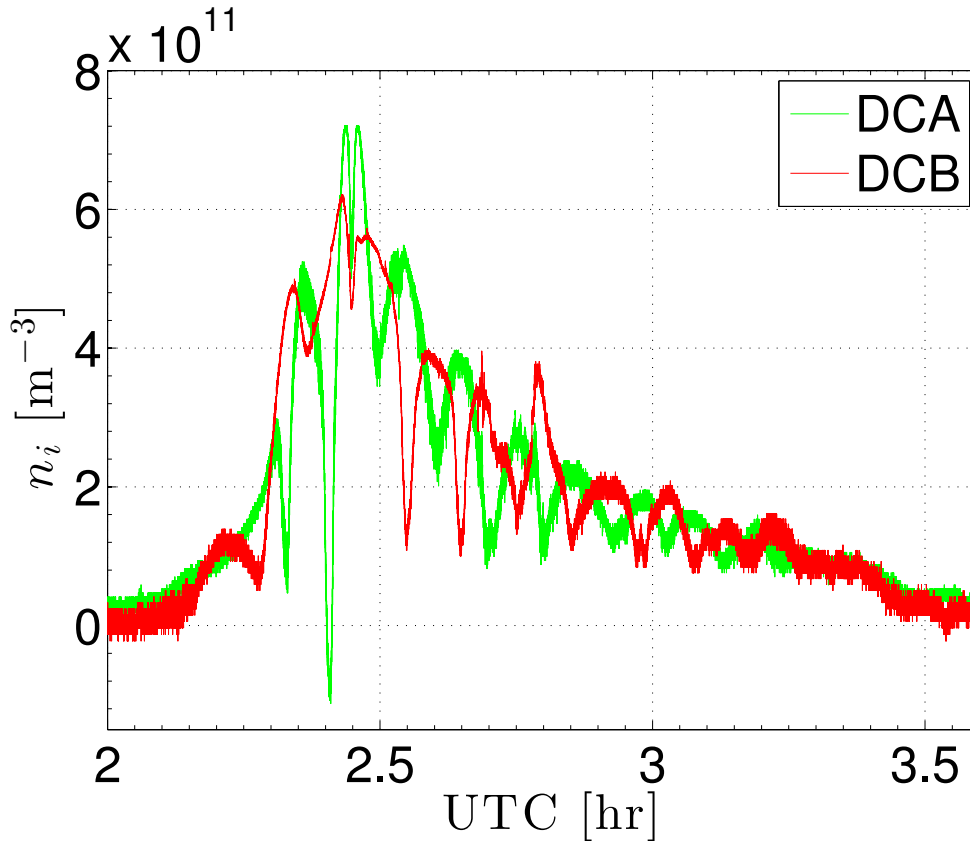
Figure 3.2: The spin-modulated densities measured by DCA and DCP within 2 hr and 3.6 hr UTC on May 26, 2012.

Abiding by the PLSV hierarchy, a simple CubeSat geometry free from external appendages and differential electrical structures is created in Gmsh as part of the SPIS preprocessing stage. The advantage of this structure is the simplicity of numerical simulation. With a spherical computational volume of radius $r = 0.75$ m ($\approx 21.5\lambda_D$), plasma dynamics within the domain may be negotiated at a moderate computational expense. The DICE CubeSat is simulated as a 10 cm $\times$ 10 cm $\times$ 15 cm (i.e. 1.5U) structure offset from the center of the computational volume by 30 cm towards the ram direction to fully display the spacecraft wake. The geometrical structure by Gmsh is illustrated in Figure 3.4.
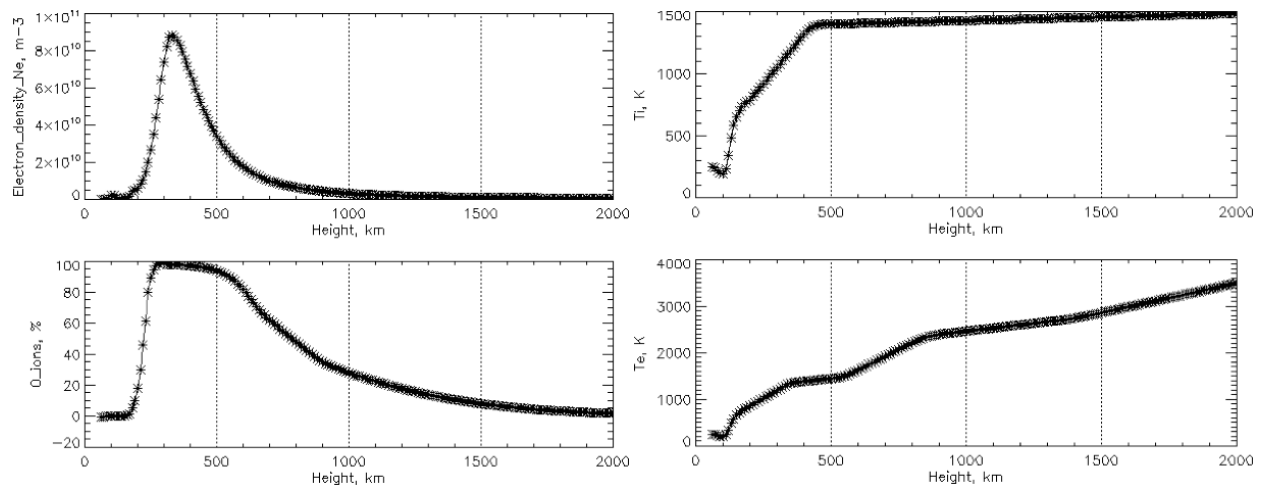
Figure 3.3: Electron density, (top left), O^+ percentage (bottom left), O^+ temperature (top right) and electron temperature (bottom right) altitude profiles at the time of interest. [*International Reference Ionosphere* (2014)]
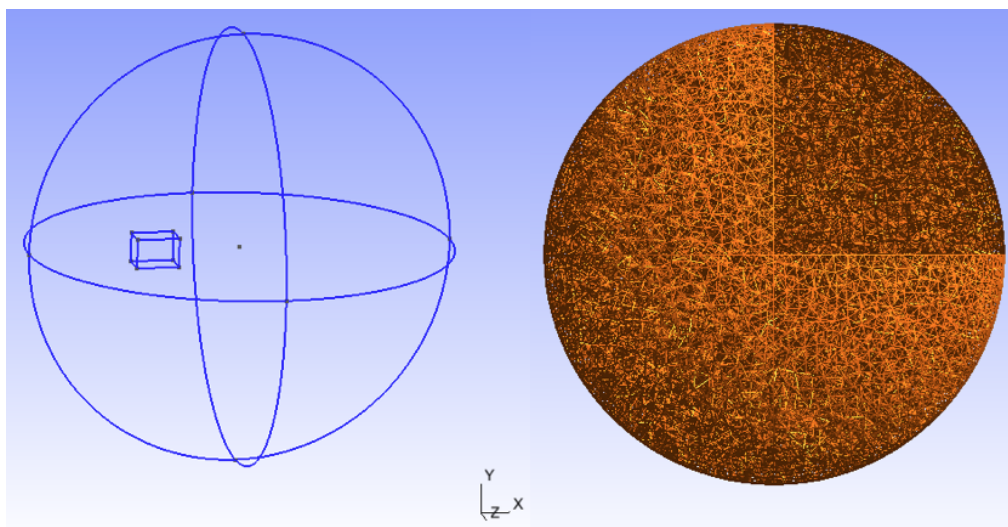
Figure 3.4: The 1.5U CubeSat within a spherical computational volume of radius $r = 0.75$ m. External appendages are not modeled.

Table 3.2: SPIS Global parameters of the DICE simulation.

Electron Volume Distribution	Global Maxwell Boltzmann
Ion Volume Distribution	PIC
Electron Density [m^{-3}]	8.09×10^9
Ion Density [m^{-3}]	8.09×10^9
Electron Temperature [K]	2065
Ion Temperature [K]	1413
Plasma Dt [s]	1×10^{-6}
Duration [s]	2×10^{-4}

Proceeding the geometrical creation of DICE, groups are allocated onto the spacecraft sur-face, external boundary and computational volume. The spacecraft surface group (ground) is aluminum with a surface temperature of 300 K. The spacecraft surface group is subject to a plasma population boundary condition and an electric field boundary condition which enables surface current balance and the computation of a surface potential, respectively. The external boundary surface group is subject to a plasma population boundary condition and electric field boundary condition such that outgoing and incoming currents may be moni-tored and plasma potentials may be computed, respectively. Since there is a single electrical node of the system represented by the spacecraft surface group, the *Electrical Circuit Editor* is bypassed.

The CubeSat is set to reside within a quasi-neutral plasma density of $n_0 = 8.09 \times 10^9$ m^{-3}. Meso-thermal conditions apply such that O$^+$ ions at $T_i = 1413$ K traveling at a spacecraft velocity of $v_{SC} = 7548.96$ m $\cdot$ s^{-1} are modeled by PIC. Although, for $v_{thi} \ll v_{SC}$, the ions are effectively stationary with respect to the moving spacecraft, SPIS simulates a stationary spacecraft in the flowing plasma. As a result, the 100 cm^2 ram surface area of the CubeSat is subject to a flux of O$^+$ particles injected with a velocity of v_{SC} at zero ram angle. Moreover, since the spacecraft is subsonic with respect to electrons at a temperature of $T_e = 2065.4$ K (i.e. $v_{SC} \ll v_{the}$) the spacecraft is immersed within the Maxwellian electron population. Magnetic fields are not included and pertinent plasma and simulation global parameters are referenced in Table 3.2.

It is noted that data visualization is not successful when using a linear Poisson solver with Maxwellian and PIC electron and ion distributions, respectively. The results that follow are reproducible when using a non-linear Poisson solver with PIC for both electrons

and ions. This, however, incurs a greater computational expense such that fine tuning is not easily performed. Although not presented in this thesis, the PIC electron case was shown to render floating potentials and wake structures seen when using Maxwellian electrons and PIC ions. Finally, several validation simulations were performed by using a variety of plasma dynamic time-steps and meshing resolutions for Maxwellian electrons and PIC ions in the non-linear Poisson solver yielding similar charging and wake structures as those that reside in the following sections. Although the non-linear Poisson solver is stable even for PIC cells larger than λ_D and *plasmaDt* values larger than ω_p^{-1}, such user inputs were selected to reduce computational expense and capture all plasma dynamics at characteristic length scales. In short, all variations of particle distributions with linear and non-linear Poisson solvers were exhausted with a wide variety of spatial and temporal resolutions. In what follows, the most economical parameterization is presented: Maxwellian electrons and PIC ions in the non-linear Poisson solver with meshing resolution on the same order of magnitude as λ_D and global plasma dynamic time-steps on the same order as ω_p^{-1}.

3.2   DICE Surface Charging

As shown in Chapter 2, ionospheric spacecraft charging in the absence of electron/ion beams, tethers or highly electrically differentiated external spacecraft components for larger spacecraft in the ionosphere is typically minor. Plasmas in the ionosphere produce small Debye lengths due to low temperatures and high densities such that the thin-sheath model of probe theory describes interactions with larger spacecraft. However, the thick-sheath model is appropriate in the ionosphere for 1.5U CubeSats. In LEO, the sheath and wake structure of a CubeSat is more complex than that of a larger spacecraft. In this section, it is shown that OML analysis is consistent with SPIS-generated surface currents on DICE.

3.2.1   Current Balance

By design, DICE is a single electrical node immersed in a meso-thermal plasma such that negative charging quickly ensues. The charging of a conducting spacecraft in a flowing plasma is analogous to one in a non-flowing plasma as $\phi_f \neq \phi_f(n_0)$, $\phi_f = \phi_f(T_e, T_i)$, $\tau_C \propto (T_e, T_i)$ and $\tau_C \propto n_0^{-1}$. Surface current balance of DICE is illustrated in Figure 3.5.

Similar to a stationary spacecraft in the plasma environment, the surface potential floats with respect to the plasma at a charging onset time τ_C defined as the time when the total surface current is neutralized. The floating potential of $\phi_f = -0.67$ V is achieved at a

minimum net current at $\tau_C \approx 5.20 \times 10^{-5}$ s.

Although the OML regime is traditionally reserved for probes in tenuous plasmas where the charged particle orbital motion radius (effectively $n\lambda_D$) in the presence of the biased probe is non-negligible with respect to the probe dimension, plasma interactions of a 1.5U CubeSat in LEO abides by the thick-sheath limit. Charged particles in LEO lack the energy to generate secondary and backscattered electrons such that surface charging due to thermal currents occurs well within a few volts while internal charging is essentially non-existent. In the absence of solar flux, spacecraft float to negative potentials with respect to the plasma as dictated by the current balance equation. In realistic conditions, ϕ_f is constantly fluctuating.
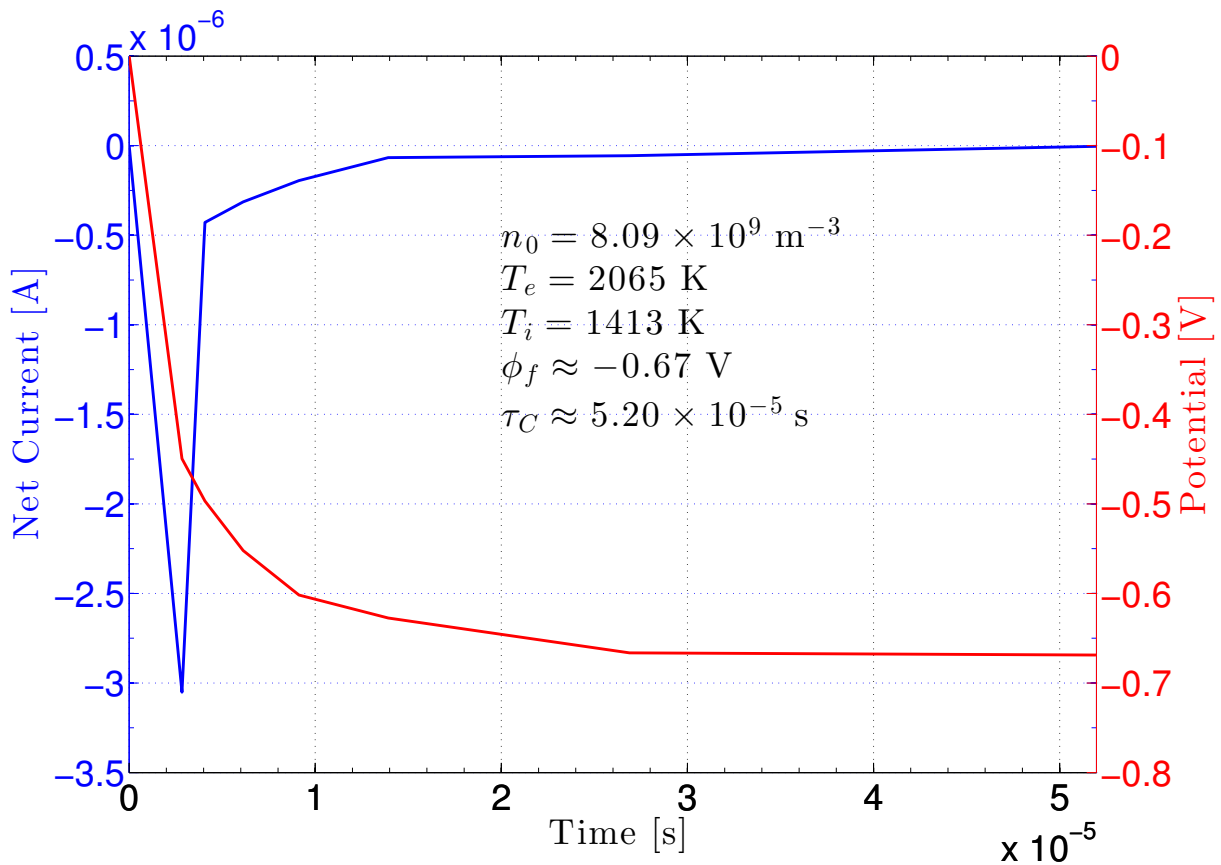
Figure 3.5: The time of charging onset $\tau_C \approx 5.20 \times 10^{-5}$ s is defined as the time of minimum absolute net current. At τ_C the DICE floating potential is $\phi_f \approx -0.67$ V.

3.2.2   Thick-Sheath Approximation

A Maxwellian electron population contributes to the net surface current of DICE by Boltzmann's repulsion factor in Equation 1.14; isothermal electrons are guaranteed in this environment as the flow is meso-thermal and collisionless. Similarly, the positive surface current contributions are purely thermal currents, which for $v_{thi} \ll v_{SC}$, are effectively ram currents estimated by Equation 1.11. Positive charge only accumulates on the DICE-F ram surface of area A_r, which is a planar surface such that $\alpha = 0$. Accordingly, the net surface current that allows DICE to float negative abides by Equation 1.15:

$$I(\phi_f) = I_i(0)\eta - |I_e(0)| \exp\left(-\frac{q_e\phi_f}{k_B T_e}\right), \tag{3.1}$$

where $I_i(0) = A_r n_0 q_i v_{SC}$ is the ion flux current, $A_r = 0.01$ m^2 is the DICE ram surface area, $\eta \approx 1.1$, $I_e(0) = A n_0 q_e v_{the}$ is the electron flux current and $A = 0.08$ m^2 is the total DICE surface area. An analytical expression for the floating potential follows from the above where $I(\phi_f) = 0$:

$$\phi_f = -\frac{k_B T_e}{q_e} \ln\left(\frac{\eta I_i(0)}{|I_e(0)|}\right), \tag{3.2}$$

Note that if $A_r \to A$, as for planar Langmuir probes, the argument of the above logarithm becomes $\eta \gamma_e^{-1}$. Equation 3.2 gives $\phi_f = -0.54$ V which is in tolerable agreement with the SPIS rendered value of $\phi_f \approx -0.67$ V considering the fact that ions reach surfaces adjacent to the ram surface by OML effects such that A_r is in fact slightly greater. Nevertheless, the net surface current on DICE according to Equation 3.1 is $I(\phi_f) = 1.32 \times 10^{-23}$ A ≈ 0 and the thick-sheath limit is suitable for DICE.

The electron current collected on DICE-F surface is given by $I_e = |I_e(0)| \exp\left(-\frac{q_e\phi_f}{k_B T_e}\right)$ or $|I_e| = 1.08 \times 10^{-7}$ A. The ion flux surface current given by $I_i = \eta A_r n_0 q_i v_{SC}$ is $I_i = 1.08 \times 10^{-7}$ A. The analytical electron current value is at an absolute error of 4.53×10^{-8} A to the electron current rendered by SPIS at τ_C, namely, $|I_e| = 1.53 \times 10^{-7}$ A. In similar spirit, the analytical ion current value resides at a 7.43×10^{-8} A absolute error from the SPIS-rendered ion current, $I_i = 1.82 \times 10^{-7}$ A. The small differences between distinct currents verify that indeed the OML regime is adequate for describing DICE-F as a Langmuir probe. Furthermore, SPIS produces consistent results for spacecraft charging in meso-thermal plasma conditions.

3.3   Plasma Wake of a CubeSat

Plasma density measurements by Langmuir probes aligned with the spacecraft velocity vector are typically reduced to those recorded by ram-side probes– ion density depletions reside in the near-wake for $\gamma_i < 1$. Measured ion depletions downstream spacecraft are neglected in favor of ram-side detections and plasma densities are traditionally taken as the greater of the two. This section states that a re-evaluation of traditional data reduction is necessary when considering the plasma wakefield structure of a 1.5U CubeSat in LEO. In particular, an ion focus region is generated.

3.3.1   Wake Structure

During the selected DICE event, plasma interactions acquire steady-state conditions within a milli-second of interaction. At τ_C, the plasma potential field is effectively steady-state with corrections for minor and incessant fluctuations in ϕ_f and the wake structure is mature. Figure 3.6 denotes a slice of the plasma potential by the *Cutting plane* filter of the SPIS post-processor through the center of DICE along the direction of plasma flow at 2×10^{-4} s from simulation initialization. At this time the CubeSat has charged to a floating potential of $\phi_f \approx -0.67$ V and the surrounding plasma potential is subsequently perturbed.
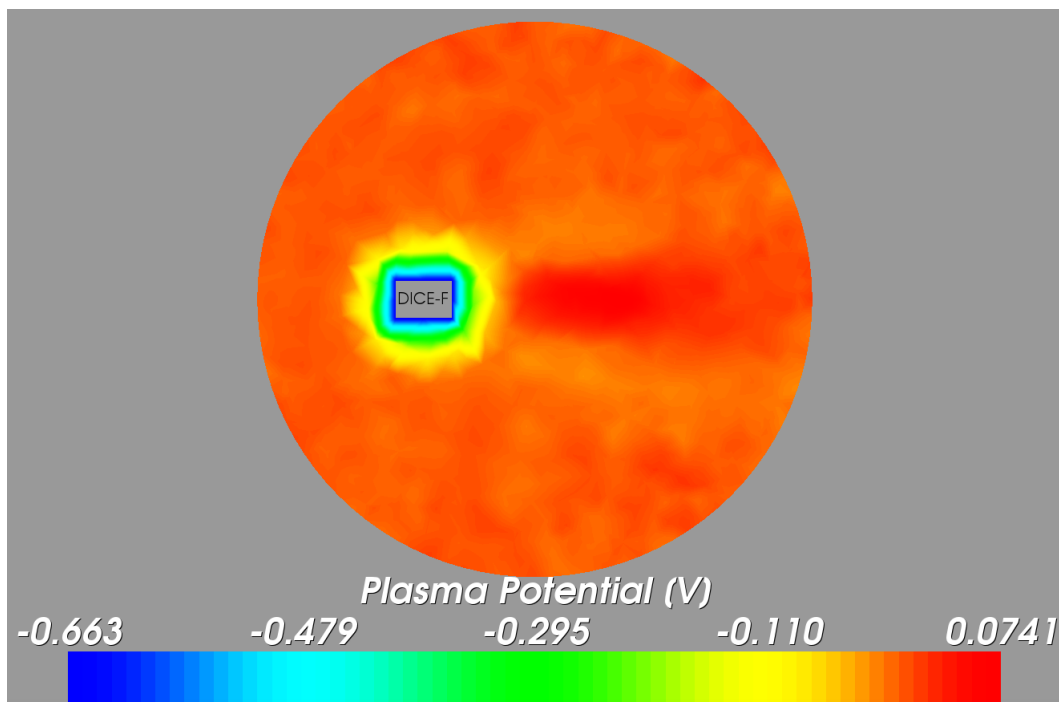

Figure 3.6: The plasma potential surrounding DICE as viewed by the *Cutting plane* filter.
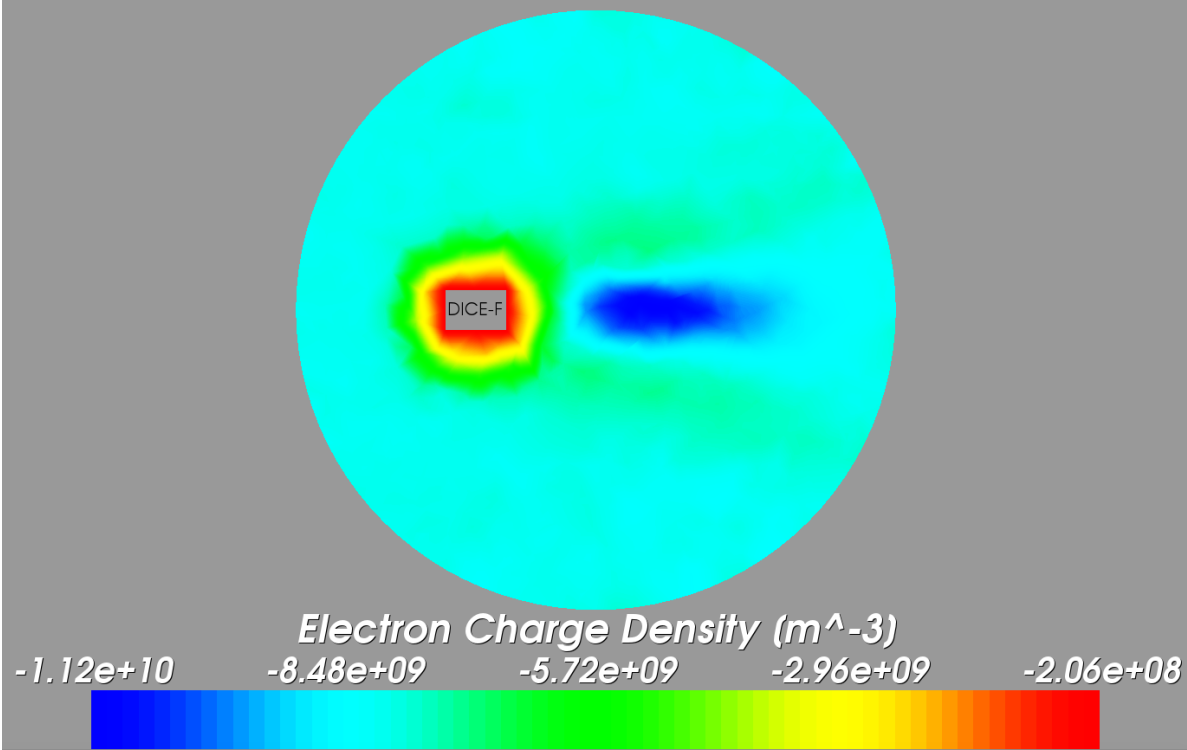
Figure 3.7: The electron charge density surrounding DICE as viewed by the *Cutting plane* filter.
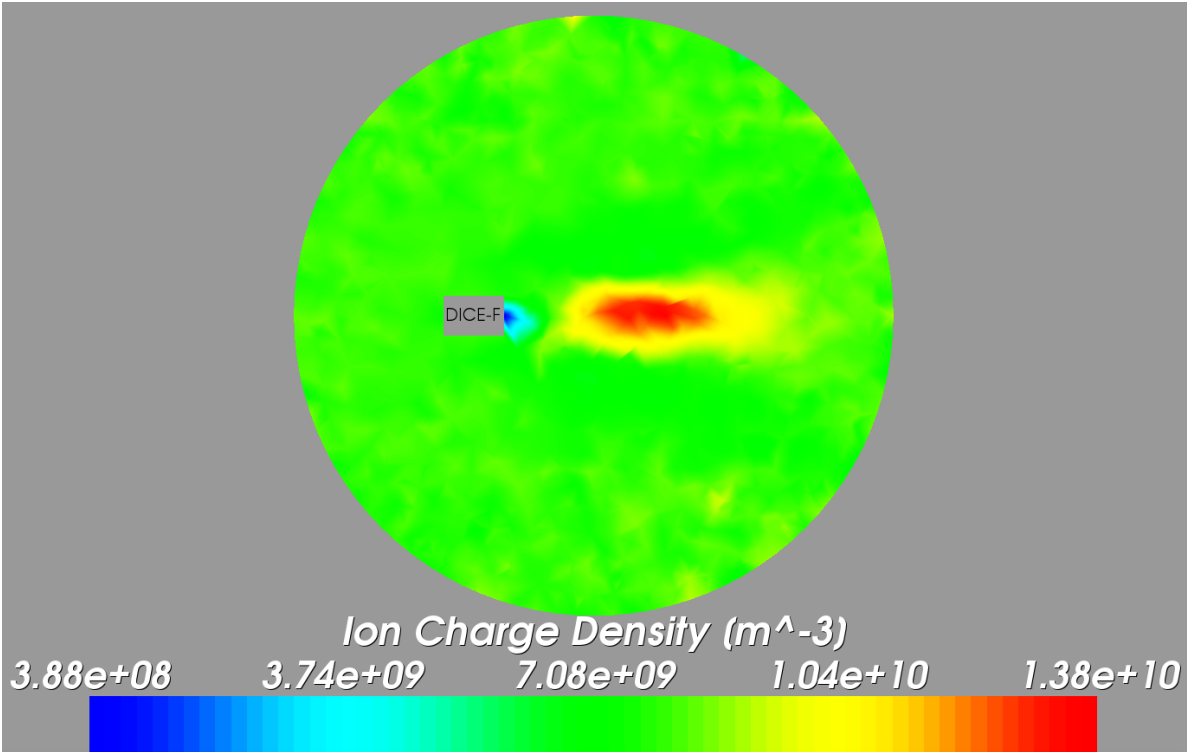
Figure 3.8: The ion charge density surrounding DICE as viewed by the *Cutting plane* filter.

The immediate anti-ram wake is what is referred to as the near-wake. The near-wake experiences a negative plasma potential which repels supersonic electrons. The high energy tail of the ion velocity distribution deems a small population of ions in the near-wake. This is best seen by the nonzero ion density in the near-wake of Figure 3.8. The extended wake-field is the far-wake where a significant number of ions have neutralized the potential field downstream and generated an ion focus region. The far-wake consists of an ion density enhancement and, by virtue of ambipolar interactions with neighboring electrons, an electron density enhancement as seen in Figures 3.7 and 3.8.

The electron density is seen to decrease with proximity to the negatively charged spacecraft in a behavior consistent with the non-flowing sheath model. Electron thermal velocities vastly exceed the bulk plasma velocity such that electron densities are dominated by electrostatic effects in the near-wake. Ion trajectories are modulated in the presence of the negatively charged CubeSat and accumulate in the far-wake. The ion focus region is of principal concern for the development of Langmuir probes for CubeSats.

3.3.2 Density Enhancement in the Far-Wake

Negatively charged Langmuir probes or small satellites of dimensionality comparable to $n\lambda$ modulate the trajectories of incoming ions by electrostatic attraction. This is a direct result of OML probe theory. The formation of an ion focus region downstream negatively charged conductors is of significant concern when developing small satellite Langmuir probes aligned along the velocity vector; Langmuir probes in the ion focus region will measure an ion density enhancement over the background level.

Spatial profiles are extracted from SPIS via *Probing line* filters applied through the central DICE axis parallel and perpendicular to the flow. Figures 3.9 and 3.10 shows *Probing line* filters as applied to the density and potential values in the computational volume perpendicular and parallel to the spacecraft velocity vector, respectively.

It is noticeable that a non-stationary CubeSat yields sheath profiles comparable to the analytical result perpendicular to the spacecraft direction of motion. Specifically, the profiles perpendicular to the propagation vector highly resemble those presented in the analytical model. For a zero ram angle, quasi-neutrality along the y-axis is achieved at equal distances of $n\lambda_D$ from the spacecraft.
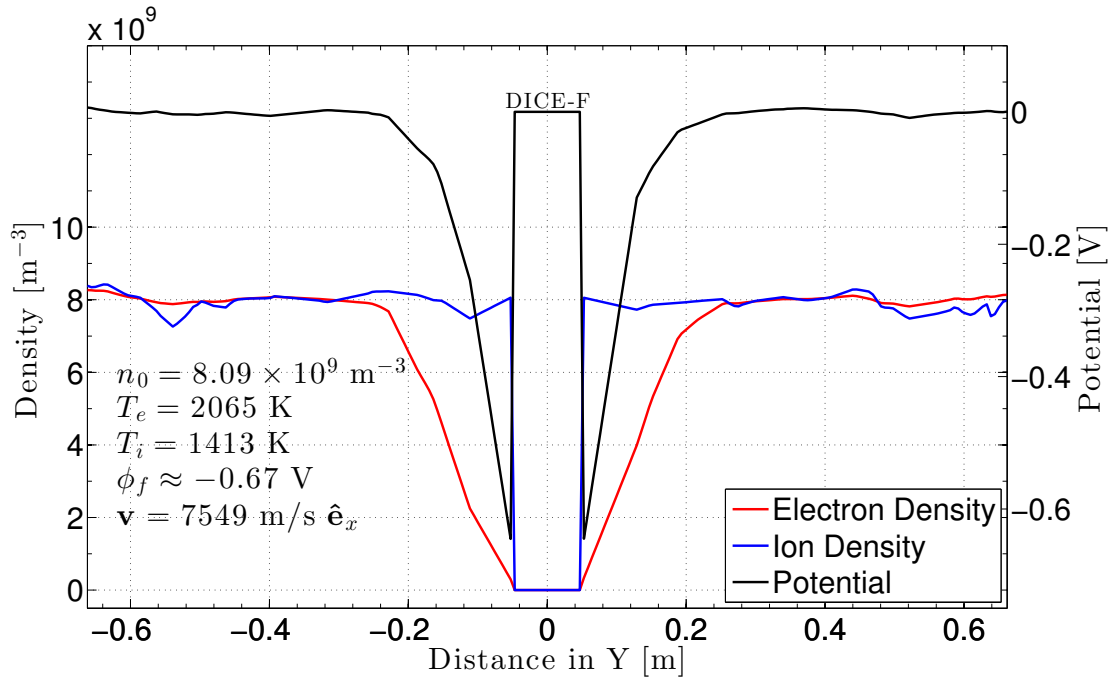
Figure 3.9: Plasma density and potential profiles perpendicular to the DICE velocity vector.
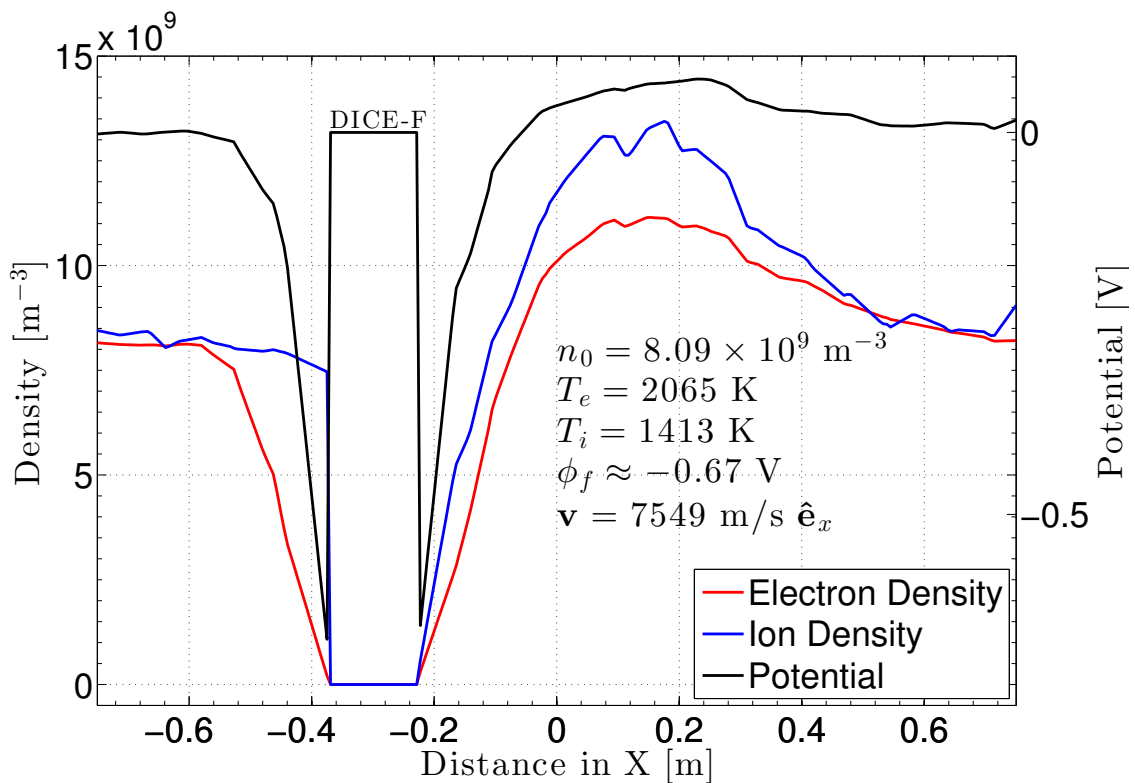
Figure 3.10: Plasma density and potential profiles along the DICE velocity vector.

The sheath thickness upstream the CubeSat along the velocity vector is compressed while it is elongated downstream the CubeSat. Perhaps more significantly, the plasma potential is positive in the far-wake. For $\gamma_e > 1$ and $\phi_f < 0$, the electron density is lower than the ion density within $n\lambda_D$ on the ram-side and wake-side sheaths alike. The electron density is enhanced over nominal in the far-wake as electrons are brought in by ambipolar electric fields.

The near-wake resides within 27 cm ($\sim 7\lambda_D$) from the DICE-F wake-side surface. The far-wake is seen to distend 88 cm ($\sim 25\lambda_D$) downstream DICE-F before the background plasma density ensues. The ion focus region begins 27 cm downstream the satellite and extends for 61 cm ($\sim 17\lambda_D$) or, equivalently, $4\ell_\parallel$ ($6\ell_\perp$) for DICE-F dimensionality parallel (perpendicular) to the direction of motion $\ell_\parallel = 15$ cm ($\ell_\perp = 10$ cm). It is also noted that a local potential maxima of $\phi \approx 0.07$ V exists in the focus region 17 cm ($\sim 5\lambda_D$) downstream the density maximum (i.e. 60.35 cm downstream the CubeSat). This is in agreement to what has previously been shown for focus regions of dust particles [Lampe et al., 2005].

DCA and DCB probes aboard DICE-F should record plasma densities of 8×10^9 m^{-3} and 8.53×10^9 m^{-3}, respectively, according to SPIS. At the DICE-F time of interest $n_{0DCA} > n_{0DCB}$ such that, according to ion focus theory, DCA is thought to trail DICE-F. As a result, it is believed that the probe positions along the propagation vector would not yield a higher DCA density had DICE-F not been tumbling. The lack of an attitude solution of DICE-F also deems the refinement of IRI parameters unsubstantiated.

The ion focus region denotes an ion density enhancement of about 66% over n_0. Quasineutrality is recuperated downstream once ion trajectories are dominated by thermal velocity components towards the axis of the velocity vector and free of electrostatic influences from the negatively charged CubeSat. The electrostatic generation of the ion focus region as rendered by SPIS is central to this investigation and independently verified in the following chapter.

Chapter 4

SPIS VALIDATION IN THE FAR-WAKE

The generation of an ion density enhancement in the ion focus region is of significant concern when determining the position of CubeSat Langmuir probes aligned with the spacecraft velocity vector. Although DICE is tumbling in the absence of an attitude solution such that the density profiles from DCA and DCB oscillate in relative density (see Figure 3.1), SPIS simulations have shown that a 1.5U CubeSat wake structure in LEO abides by OML probe theory. This claim is further validated for analytical current balance relations in the thick-sheath approximation. In this chapter, the ion density enhancement in the far-wake as rendered by SPIS is replicated by an independent MATLAB code.

4.1   SPIS Simulation of a Spherical Spacecraft

4.1.1   Simulation Parameterization

SPIS is currently regarded as a premier spacecraft charging package that continues to gain popularity throughout the world. In particular, SPIS is capable of generating wakefields in a plasma for detailed spacecraft geometries. In an attempt to independently validate SPIS results, however, a simple spherical spacecraft geometry is considered. A spherical spacecraft facilitates the analytical computation of a plasma potential as edge effects are significantly minimized.

The radius, $r = 9$ cm, of the spherical spacecraft is selected for SPIS simulation such that it may justly encapsulate a DICE CubeSat. Geometrical groups consist of a spacecraft surface group, external boundary group and a volume group.

Table 4.1: SPIS global parameters for the spherical spacecraft model.

Electron Volume Distribution	Global Maxwell Boltzmann
Ion Volume Distribution	PIC
Electron Density [m^{-3}]	8.09×10^9
Ion Density [m^{-3}]	8.09×10^9
Electron Temperature [K]	2065
Ion Temperature [K]	1413
Plasma Dt [s]	1×10^{-6}
Duration [s]	1×10^{-3}

For consistency, boundary conditions placed on groups of the spherical model are those applied onto groups of the DICE model as overviewed in the previous chapter. The aluminum spherical spacecraft is centered 30 cm upstream the flow of plasma in a spherical computational volume of radius $r = 0.75$ m as seen in Figure 4.1. The sphere is modeled without external appendages as a solitary electrical node such that a non-biased floating potential of $\phi_f \approx -0.62$ V is attained at τ_C. From Equation 3.2, $|\phi_f| \propto A_r/A$. Since the sphere charges to a lower magnitude than DICE in similar conditions, it is led to believe that by geometry, A_r/A is greater for DICE than the sphere when taking into consideration ion flux on surfaces greater A_r as given by OML theory.
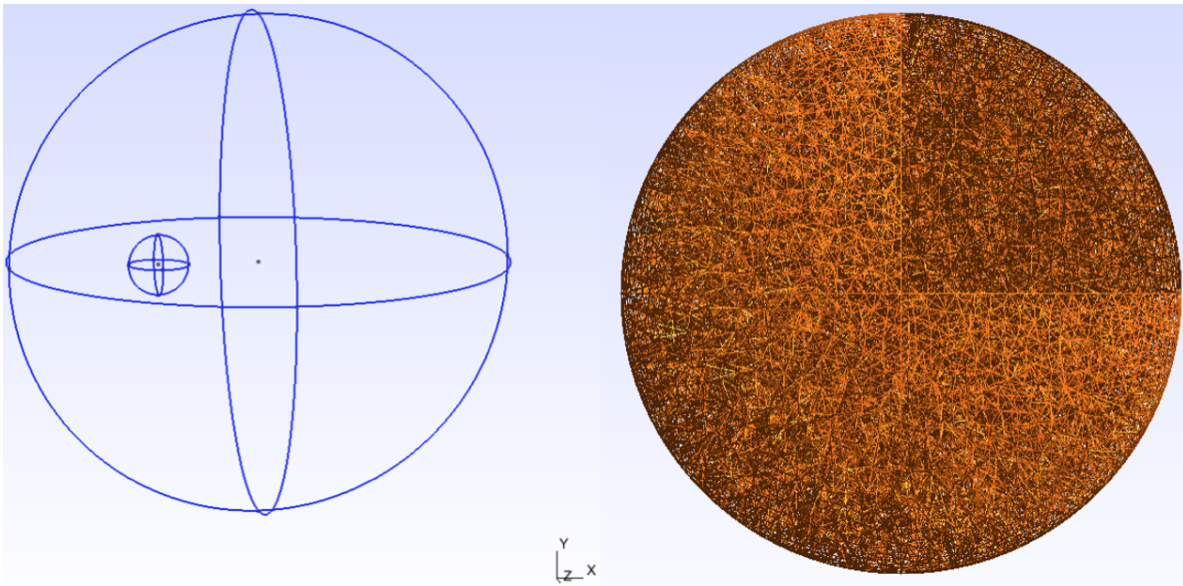
Figure 4.1: The spherical spacecraft geometry selected to reduce edge effects in the potential field.

The τ_C dependence on surface area, A, is not numerically verified in this investigation although it is assumed that for constant n_0, $\tau_C \propto A^{-1}$ as $\tau_C \propto \phi_f$. Table 4.1 tabulates plasma and simulation parameters allocated onto the spherical model that mimic those of the DICE model. The satellite is set to travel at the same v_{SC} as DICE and only O^+ ions are considered. As with the previous simulations, the *plasmaDt* parameter is chosen to be of the same order of magnitude as ω_p^{-1} although a nonlinear Poisson solver is employed in SPIS-NUM for a Maxwellian (PIC) electron (ion) distribution.

4.1.2 Wake Structure

By design, the spherical spacecraft model exhibits a wakefield similar to that of the DICE CubeSat. A negative plasma potential resides in the ram-side sheath and near-wake in a result granted by exponentially decaying plasma potential with distance of Equation 1.4 as seen in Figure 4.2. In such regions, the total charge density is generally positive by electrostatic attraction of ions. The on-axis near-wake, however, is dominated by the high energy tail of the electron distribution function. The electron dominance in this region is suspected to be further assisted by ambipolar interactions with the high energy population of the ion distribution function, that is, the population of ions with sufficient thermal energy to inhabit the near-wake. This behavior is consistent with the DICE wake structure in meso-thermal conditions and may be verified in Figures 4.2, 4.3 and 4.4.
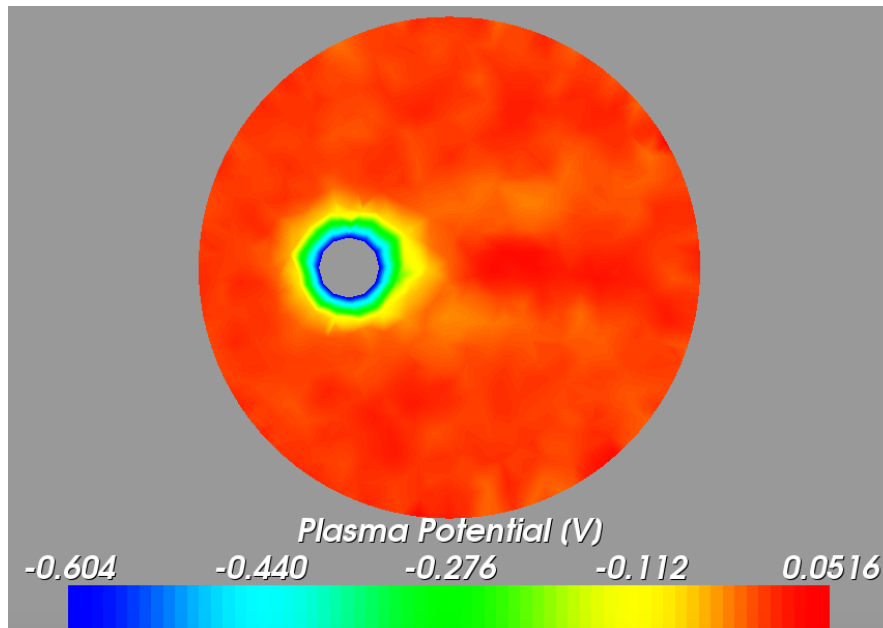
Figure 4.2: The plasma potential surrounding the spherical spacecraft as viewed by the *Cutting plane* filter.

Figure 4.3: The electron charge density surrounding the spherical spacecraft as viewed by the *Cutting plane* filter.

Figure 4.4: The ion charge density surrounding the spherical spacecraft as viewed by the *Cutting plane* filter.

Figure 4.5: Plasma density and potential profiles perpendicular to the spherical spacecraft velocity vector.

Figure 4.6: Plasma density and potential profiles parallel to the spherical spacecraft velocity vector.

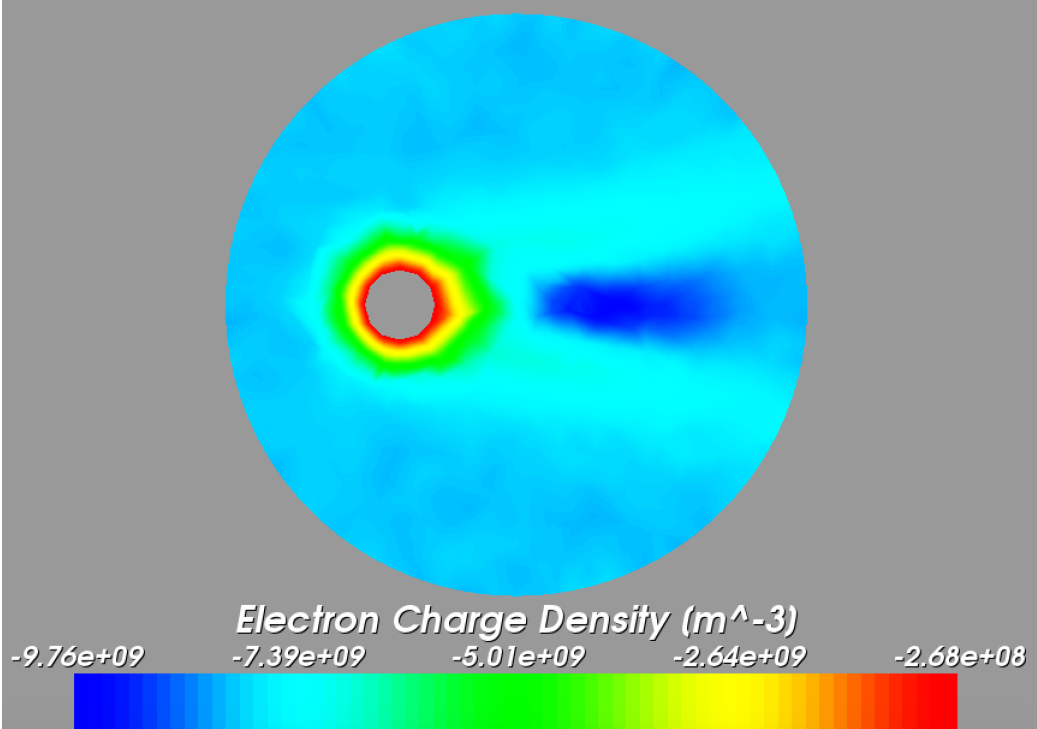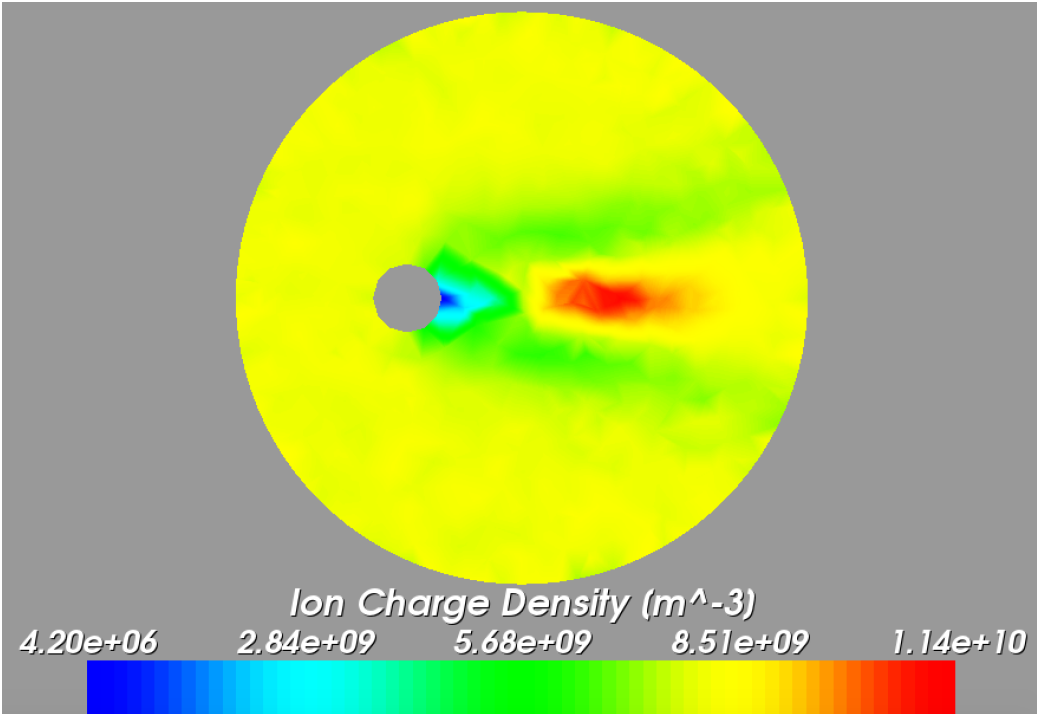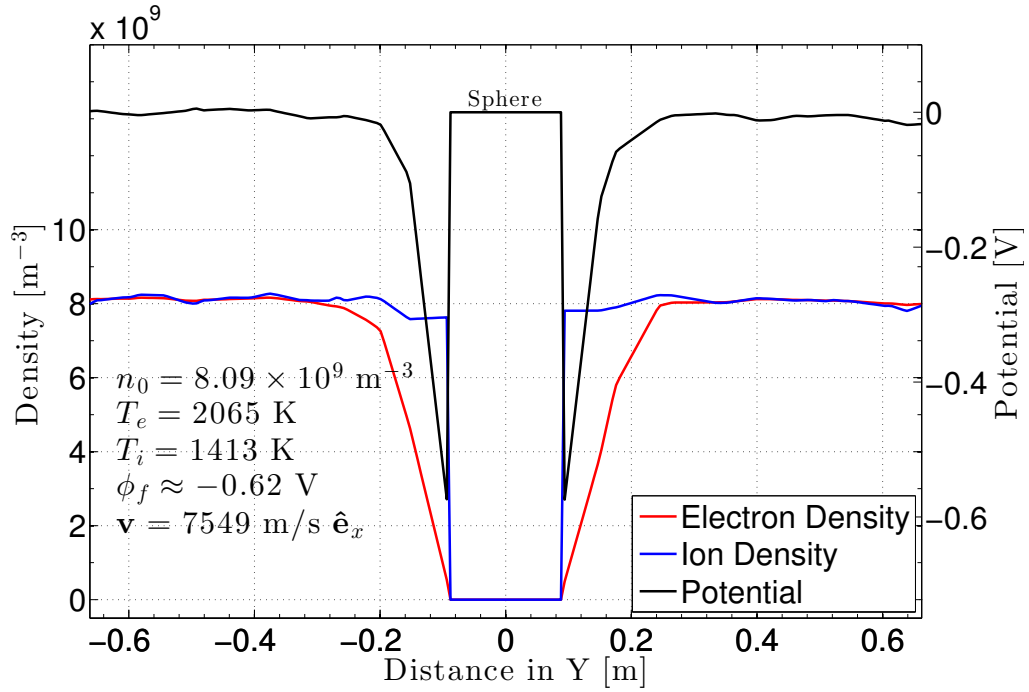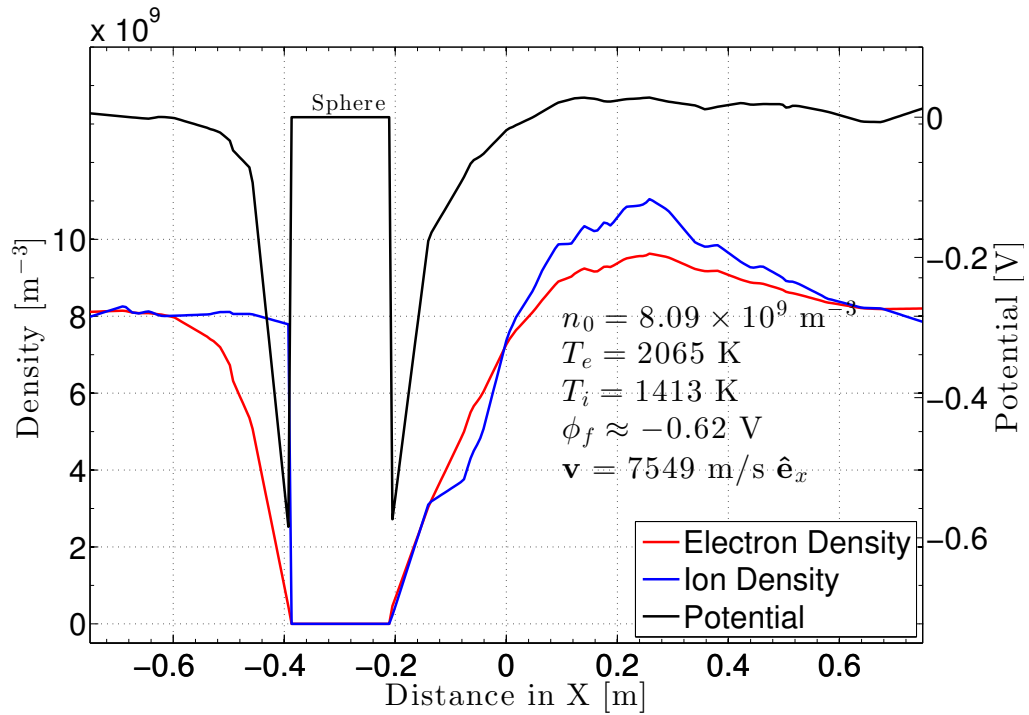As before, spatial plasma profiles are extracted by the *Probing line* filter of the SPIS post-processor applied perpendicular and parallel to the spacecraft velocity vector and through the center of the sphere. It is noticed that for a spacecraft offset from the origin in a spherical domain, zero variable values are given by the *Probing line* filter beyond the external boundary. The sheath structure surrounding the spherical spacecraft model perpendicular to the direction of flow is consistent with the analytical model of Figure 1.1.

The sheath thickness of Figure 4.5 is seen to extend a distance equal to $n\lambda_D$ along this component of the DICE-F model since λ_D is independent of spacecraft geometry. Along the direction of flow, the near-wake is within 23 cm of the satellite and quasi-neutrality is achieved ≈ 89 cm ($\sim 25\lambda_D$) downstream the spherical spacecraft. The ion focus region begins 23 cm downstream and extends for 58 cm ($\sim 17\lambda_D$) or, equivalently, 4ℓ for spacecraft diameter $\ell = 18$ cm. The ram-side sheath structure agrees well with theory.

Although the geometry of the wake structure for the spherical model is in close agreement to that generated by the DICE CubeSat, the maximum ion density in the ion focus region generated by the spherical spacecraft exceeds the background density, n_0, by 36%. This leads one to consider the role that satellite geometries play in the degree of ion lensing- the DICE CubeSat displays a density enhancement of 68% over nominal. The justification of this claim, however, is best reserved for future studies.

4.2   MATLAB Simulation of the Far-Wake

A two-dimensional MATLAB code was developed to validate the far-wake ion density enhancements rendered by SPIS on a per-particle basis. Ion trajectories are modeled in the particle reference frame such that the spherical spacecraft is stationary; particles are released at v_{SC} along the x-axis and v_{thi} perpendicular to v_{SC}. A plasma potential field is generated via Equation 1.4 which modulates trajectories of ions for $\phi_f \neq 0$.

The spherical spacecraft model has a radius of $r = 9$ cm and is placed at the origin. O^+ ion positions are updated in 5×10^{-11} s time-steps in the presence of $\phi_f \approx -0.62$ V while gravitational effects are negligible. The spacecraft is at the origin such that the ion position vector is $\mathbf{r}_i = x\hat{\mathbf{e}}_x + y\hat{\mathbf{e}}_y$ which is thus the separation vector between the ion and spacecraft. The potential field at the ion, ϕ_p, is proportional to the e-fold decay of ϕ_f (i.e. $\phi_p \propto \phi_f e^{-r_i/\lambda_D}$) in accordance to the Debye-Hückel potential of Equation 1.4.

It is seen by Figure 4.7 that the potential as a function of distance in the near-spacecraft

environment is dominated by the exponential decay of the potential. The exponential contribution to the potential falls off much faster than the inverse distance term such that, in the sheath, the inverse distance term is negligible.

Although, the inverse distance potential reaches zero at a distance further from the surface than the exponential potential, at this location the potential has already decreased to zero by the exponential term. As a result, at the Debye length of $\lambda_D = 3.5 \times 10^{-2}$ m the decaying exponential term defines the sheath thickness as seen in Figure 4.7:

$$\phi_p \approx \phi_f \exp\left(\frac{-r_i}{\lambda_D}\right). \tag{4.1}$$
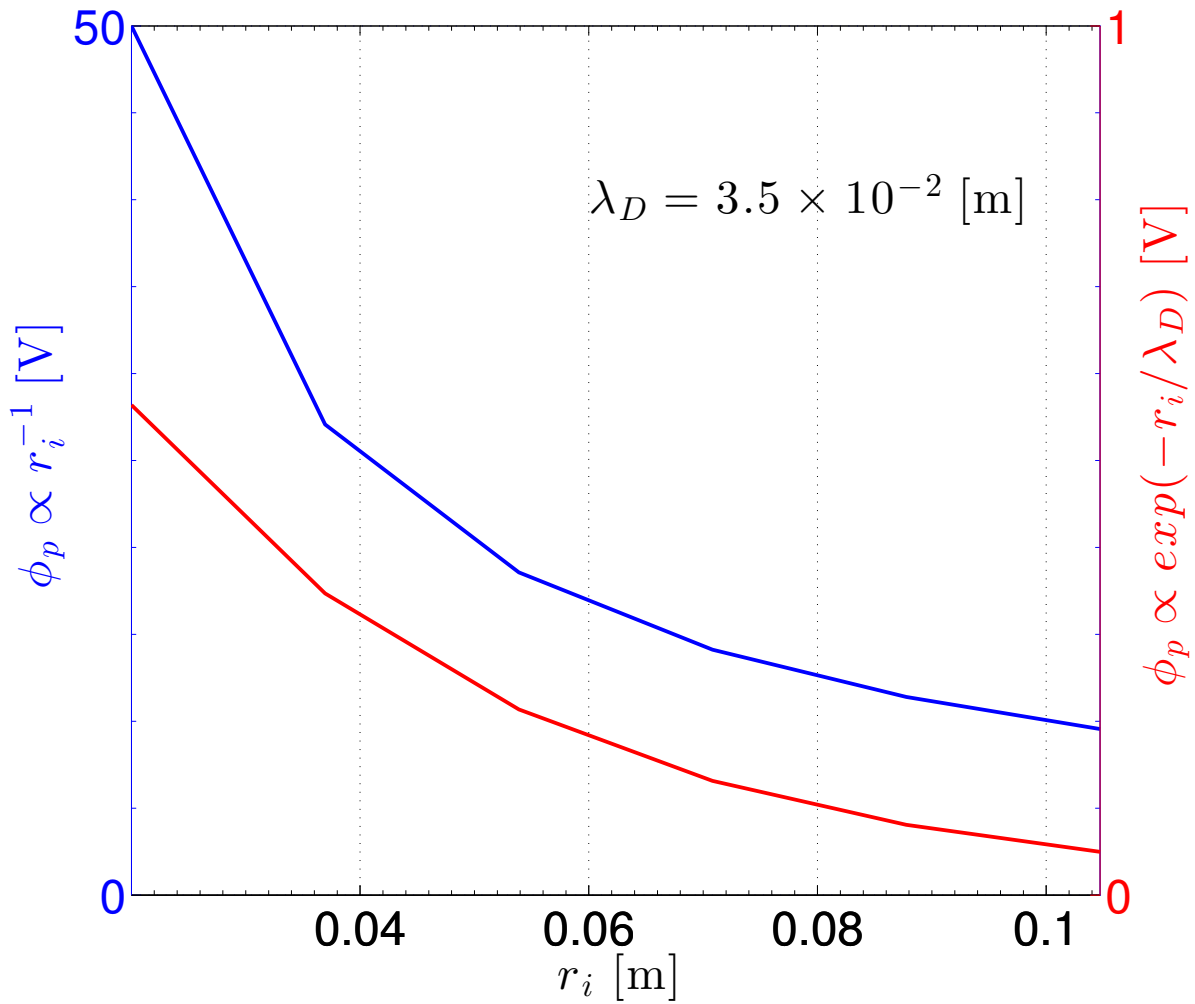
Figure 4.7: The plasma potential is limited by the exponential decay at $\lambda_D = 3.5 \times 10^{-2}$ m. r_i values are those through the center of the spherical spacecraft perpendicular to the flow extending from 2 cm $\leq r_i \leq 3\lambda_D$.

The ion acceleration, $\mathbf{a}$, towards the spacecraft is due to the electric field along r_i with a magnitude:

$$a = \frac{q_i}{m_i}\frac{\phi_p}{r_i}. \tag{4.2}$$

In index notation, where an acceleration component is a_j and ion initial (final) positions and velocities are r_{ij} (r_{fj}) and v_{ij} (v_{fj}) for $j = x$, y, respectively, the trajectory of an ion follows from classical kinematic relations:

$$\begin{pmatrix} r_{fj} \\ v_{fj} \end{pmatrix} = \begin{pmatrix} r_{ij} + v_{ij}t + \frac{1}{2}a_jt^2 \\ v_{ij} + a_jt \end{pmatrix}, \tag{4.3}$$

where t is the time-stamp in 5×10^{-11} s increments. Ion kinematics are updated during each time-step for iteration. During each iteration, a potential, force and resulting acceleration is computed such that the above kinematic relations may trace the particle trajectory for given velocities and positions. This two-dimensional model only simulates O^+ trajectories yet may easily be extended to accommodate multiple species in three dimensions.

4.2.1 Thermal Wake

In context of the geometric wake, a MATLAB simulation is performed for an uncharged spherical spacecraft. Particle motion is initiated by a bulk flow velocity, v_{SC}, and a thermal velocity, v_{thi} towards the wake axis (i.e. the x-axis) such that $\mathbf{v}_i = v_{SC}\hat{\mathbf{e}}_x \pm v_{thi}\hat{\mathbf{e}}_y$.
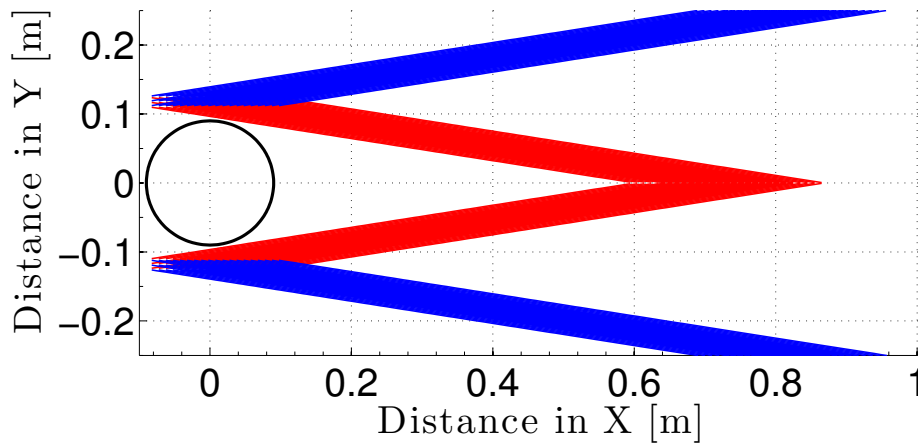
Figure 4.8: The thermal plasma wake of an uncharged sphere with thermal velocities away from the wake-axis (blue) and towards the wake-axis (red). This is the traditional view of plasma wakes in the ionosphere.

Ions are initialized at discrete positions in the computational domain; three linearly spaced values of y are selected such that 11 cm $\leq y \leq r + \lambda_D$. For each value of y are 19 linearly spaced x values from -9 cm $\leq x \leq 9$ cm in 1 cm increments. Figure 4.8 shows the thermal wake of an uncharged spherical spacecraft where the blue trajectories correspond to ions with thermal components away from the wake-axis and red trajectories correspond to the ions with thermal components towards the wake-axis.

The wake in the absence of electrostatic interactions in a meso-thermal flow is effectively a thermal wake. Although, ion thermal velocities are in random directions, it is considered here that they are either directly towards or away from the wake-axis. The ion Maxwellian velocity distribution function has a mean at v_{thi}, yet the high-energy and low-energy tail of the function is neglected in this model. The near-thermal wake is populated with high-energy ions yet in this model the near-wake is void.

Since $v_{thi} \approx 10\% v_{SC}$ for O^+, it is expected that thermal contributions will alter the the wake for uncharged and charged spacecraft alike. By triangulation, for $\mathbf{v}_{SC} \perp \mathbf{v}_{thi}$, the background plasma density is assumed to return at a distance of $\chi_t = (v_{SC}^2 + v_{thi}^2)^{1/2}$ downstream. It is seen that quasi-neutrality returns 0.5044 m downstream the satellite for $\phi_f = 0$ and $\gamma_i < 1$. Since a small number of particles are released, a density depletion is between the red and quasi-neutrality everywhere else. When solely considering the thermal wake of a CubeSat in the ionosphere, it is easily seen that density measurements by Langmuir probes aligned with the velocity vector are traditionally reduced to those detected upstream due to the density depletion in the near-thermal wake.

4.2.2   Electrostatic Wake
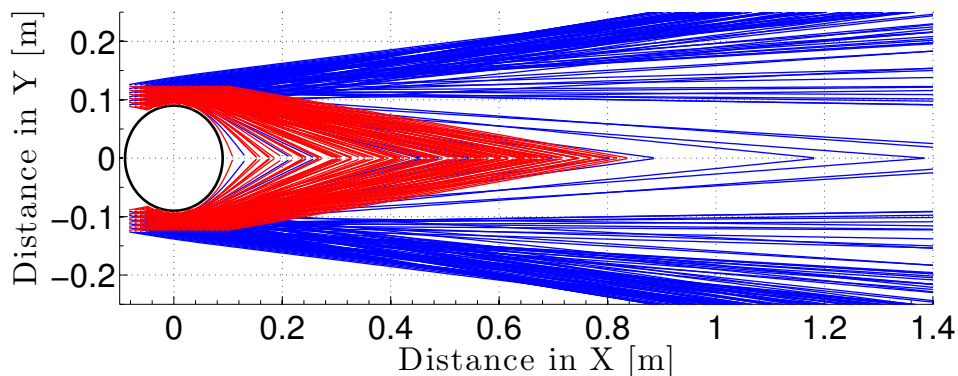
Figure 4.9: The electrostatic plasma wake of a charged sphere with floating potential $\phi_f = -0.62$ V. Ions with thermal velocities towards the wake-axis are shown in red and those with thermal components away from the wake-axis are shown in blue.

It is expected that ions within $n\lambda_D$ of the spacecraft will be influenced by the potential field at the ion, ϕ_p, for $\phi_f \neq 0$. This simulation initializes particles at six linearly spaced values y: $9 \text{ cm} \leq y \leq r + \lambda_D$. Each y value has 19 linearly spaced x values from $-9 \text{ cm} \leq x \leq 9 \text{ cm}$ in 1 cm increments. An attractive force governed by Equation 4.2 on O^+ ions of mass m_i is introduced. The wake produced by the electrostatic modulation of ion trajectories is called the electrostatic wake. Particle trajectories with v_{thi} towards the wake-axis are denoted in red while those with components away from the wake-axis are shown in blue. The negative plasma potential around the satellite is minor compared to the negative floating potential of the satellite. As such, the plasma potential is not considered.
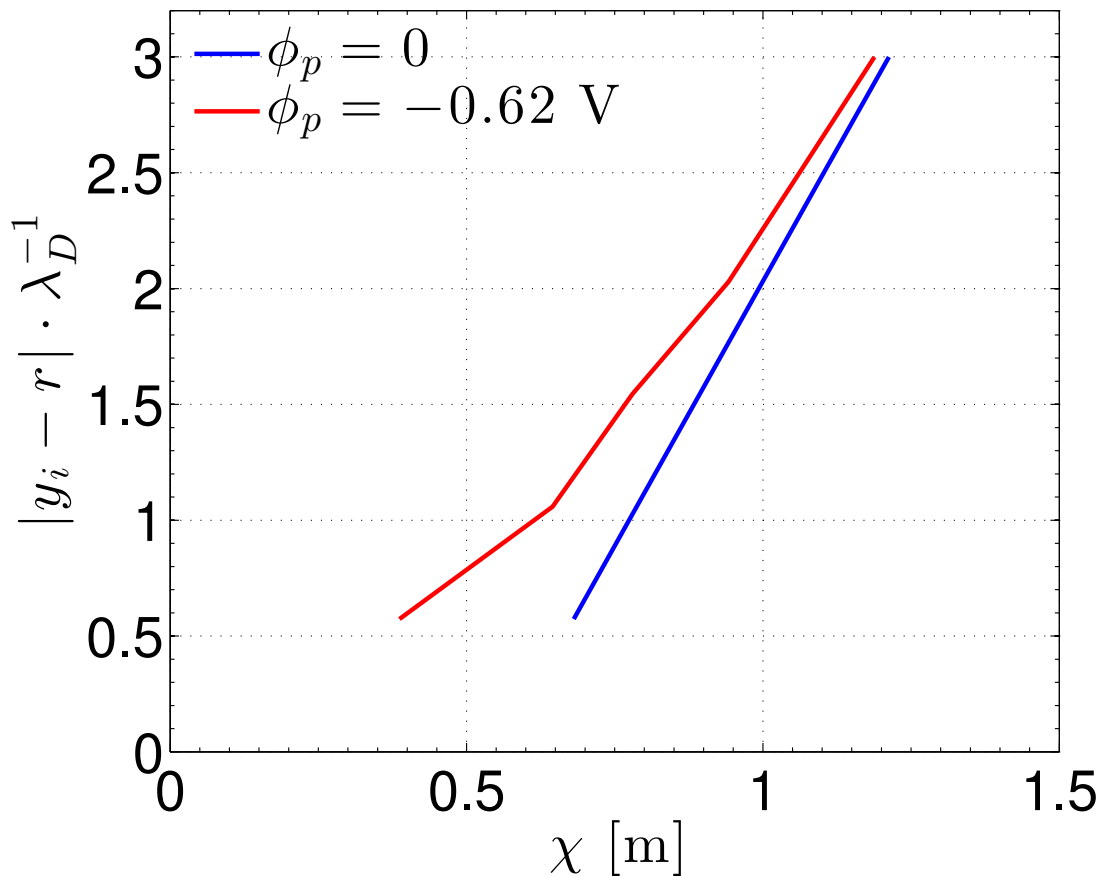
Figure 4.10: The distance from the spacecraft perpendicular to the flow and through the spacecraft center, $|y_i - r|$ as a function of focusing distance χ. Focusing distances by electrostatic lensing, χ_e, converge to focusing distances by purely thermal motions, χ_t, with greater distances $|y_i - r|$.

It is seen by Figure 4.9 that in fact some ions are collected on the wake-side surface. As seen by SPIS simulations, it is expected that high energy ions are collected on the on-axis wake-side surface. Ions reach the wake axis at distances closer to the spacecraft in the presence of $\phi_f < 0$. The negatively charged sphere focuses ions along the wake axis since the spacecraft is not irregularly shaped nor elongated. The distance that an ion reaches the wake axis relative to the spacecraft is χ. For the thermal wake (i.e. $\phi_f = 0$), $\chi_t = (v_{SC}^2 + v_{thi}^2)^{1/2}$ and in general, for the electrostatic wake, $\chi_e = |x_f - x_i|$, where x_f is the final ion position along the wake axis and x_i is the initial ion position. Thermal velocities influence the value of $\chi-$ for thermal ion motions towards the wake axis and $\mathbf{v}_{SC} \perp \mathbf{v}_{thi}$, $\chi \propto T_i^{-1}$.

Focused ions are primarily brought in from the near-spacecraft vicinity where the potential is strongly influential. The exponential decay of the sheath potential deems further ion initial positions more immune to electrostatic lensing. At $3\lambda_D$, the trajectories of particles subject to electrostatic attraction are minimally modulated. At the sheath edge of $n\lambda_D$, such trajectories are solely dominated by thermal and bulk velocities. Figure 4.10 shows how ions at far distances, $|y_i - r|$, from the spacecraft perpendicular to the flow will tend towards thermal wake structure. The ion depletion in the near-wake gradually becomes populated with distance downstream such that an approximately background density resides in the mid-wake and an enhancement in the far-wake. This effect is due to the electrostatic lensing of ions in the mid-wake and far-wake and is consistent with the SPIS result of Figure 4.4.

4.2.3 Ion Focus Region

The ion density along the wake-axis downstream the sphere may be extracted by binning particles. Since the number of particles initiated, n_0, is arbitrary, the density is best represented as a fraction of n_0. For each bin ranging 0.2 m along the wake-axis, the density profile normalized by the background density of the thermal wake shows a unit step function. More importantly, the normalized density profile of the electrostatic wake shows a density enhancement of 32% over background between 0.4 m $\leq \chi \leq$ 0.6 m which agrees well with the SPIS-rendered ion focus enhancement. This is seen in Figure 4.11.

The rudimentary plasma dynamics modeled in the MATLAB code depict a focus region in the far-wake. The MATLAB simulation shows a density depletion, enhancement and background density within 1.4 m of the satellite. An ion density enhancement of 32% over background resides between 0.4 m $\leq \chi \leq$ 0.6 m and quasi-neutrality is regained at 1.2 m $\leq \chi \leq$ 1.4 m. This is in close agreement to the $\approx$ 36% density enhancement at $\approx$ 0.4 m downstream as rendered by the SPIS model. For a low binning resolution, the

general behavior of the ion focus regions agree. This rudimentary MATLAB simulation does not consider random thermal motions, Maxwellian velocity distributions, Debye lengths, ambipolar effects and other plasma dynamics. Nevertheless, a leading order approximation of ion focus theory is presented which verifies the far-wake structure of a CubeSat in the ionosphere as rendered by SPIS.

It is shown in this chapter that the ion focus region is a reproducible phenomenon in the far-wake of CubeSats in the ionosphere. SPIS simulations consider various particle interactions beyond the scope of the rudimentary validation design, however, ion density enhancements in the far-wake exist. The validation design presented here models ion lensing in the presence of a charged spacecraft. A statistical analysis of thermal velocity vectors and a general refinement of the validation design is reserved for future work.
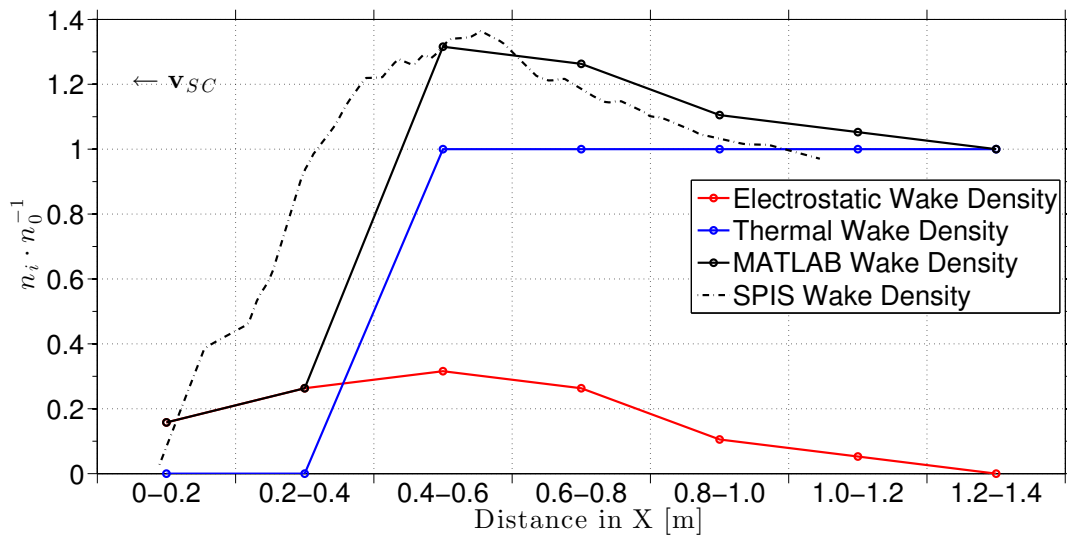

Figure 4.11: Normalized densities along the wake-axis. The binned densities of the electrostatic wake and thermal wake are in red and blue, respectively. The combined electrostatic and thermal densities show an ion enhancement of 32% above background (black). The normalized SPIS density along the wake-axis (black dash-dot) agrees well.

Chapter 5

CONCLUSION

The study of spacecraft-plasma interactions for CubeSats is currently blossoming into view. Charging effects and plasma wakes of small satellites incur a theoretical departure from thin-sheath probe theory commonly known to describe interactions of large spacecraft in LEO. Furthermore, the charging simulation package SPIS is gaining recognition as a robust tool in the world-wide spacecraft charging community.

This theses begins with an overview of the plasma frequency and Debye length in reference to PIC modeling. The concept of plasma quasi-neutrality is considered in context to Langmuir probe theory. I-V curves produced by voltage sweeping Langmuir probes are introduced and current balance relations define the concept of a floating potential. An analytical model of sheaths generated around charged conductors in a plasma is presented for a basis of comparison for numerical sheath structures. Proceeding an introduction to spacecraft charging, a traditional perspective of spacecraft plasma wakes are introduced for meso-thermal plasmas. Previous work with ion focus regions for dust grains and satellites in non-LEO conditions are overviewed. Chapter 1 concludes with an overview of the DICE mission, its instrumentation and the simulation tool SPIS.

In a preliminary analysis, SPIS is scrutinized in its capacity to model surface charging effects of a small, stationary 1.5U CubeSat in six plasma conditions characteristic of ionospheric conditions. This study numerically verifies that the spacecraft floating potential is independent of plasma density that is, $\phi_f \neq \phi_f(n_0)$. This fact is well known for surface charging in Maxwellian plasmas in the thick-sheath limit. This chapter shows that the time for currents to balance on a charged surface is proportional to plasma temperature and inverse to plasma density, that is, $\tau_C \propto T$ and $\tau_C \propto n_0^{-1}$.

Chapter 3 shows results from a SPIS simulation of a simplified DICE CubeSat model

in a moderate latitude, night-time location in LEO. Analytical current balance relations in the thick-sheath limit agree with SPIS results. Plasma wakes denote an ion density enhancement in the far-wake. This feature becomes the focus of this thesis. The simulations in this chapter reference the IRI model for plasma conditions at the time of interest. The absence of an attitude solution for DICE deems the location of the Langmuir probes with respect to the plasma wake unknown such that a refinement of ionosphere parameters by DICE is not possible. Nevertheless, SPIS simulations show ion enhancements of up to 66% above background in an ion focus region that extends $\sim 7\lambda_D$ to $\sim 17\lambda_D$ downstream DICE. Accordingly, the relative densities in the ram and anti-ram directions are of primary interest.

Paramount to this investigation is the ability of ions in the meso-thermal wake of a negatively charged CubeSat in the ionosphere to generate an ion focus region. A final SPIS simulation is performed for a spherical spacecraft such that a validation model for the same spacecraft geometry may be simplified. The spherical model is employed to reduce edge effects on the potential field in the validation design– an independently designed MATLAB model created to validate SPIS results in the far-wake. Ion density enhancements in the far-wake of SPIS simulations are successfully replicated by the MATLAB model.

The thick-sheath limit of probe theory is shown to agree with spacecraft-plasma interactions of a 1.5U CubeSat in LEO. In effect, significant ion density enhancements exist in the ion focus region of a 1.5U CubeSat in the ionosphere. Future work includes the study of geometrical dependencies on the wake-structure and a refined characterization of the ion focus region. The DICE plasma wake in LEO incurs a level of complexity not seen for larger spacecraft. Ion density enhancements should be considered during the design stage of Langmuir probes for CubeSats and wake structures should be analyzed prior to I-V curve density extraction. Langmuir probe technology must evolve as CubeSats become more prevalent and versatile. With proper design, these small explorers will have a bright future.

Bibliography

Sed. URL `http://www.haystack.edu/atm/science/coupling/sed/index.html`.

Special issue on tss-1r: Electrodynamic tether-ionospheric interactions. *Geophysical Research Letters*, 25(4-5), 1998.

Educational payload on the vega maiden flight call for cubesat proposals. Technical Report Issue 1 Revision 1, European Space Agency, Education Office, Directorate of Legal Affairs and External Relations, February 2008.

SPIS-GEO: Simplified MEO/GEO tools for spacecraft charging, 2012. 12th SCTC.

SPIS-UI, A New Integrated Modelling Environment for Space Applications, 2005. 9th SCTC.

S. D. Bale, C. J. Owen, J.-L. Bougeret, K. Goetz, P. J. Kellogg, R. P. Lepping, R. Manning, and S. J. Monson. Evidence of currents and unstable particle distributions in an extended region around the lunar plasma wake. *Geophysical Research Letters*, 24(11):1427–1430, 1997. ISSN 1944-8007. doi: 10.1029/97GL01193. URL `http://dx.doi.org/10.1029/97GL01193`.

A. Barjatya. *Langmuir Probe Measurements In The Ionosphere*. PhD thesis, Utah State University, May 2007.

P. M. Bellan. *Fundamentals of Plasma Physics*. Cambridge University Press, New York, 2006.

C. K. Birdsall and W. B. Bridges. *Electron Dynamics of Diode Regions*. Academic Press, New York, 1966.

C. K. Birdsall and A. B. Langdon. *Plasma Physics via Computer Simulation*. Institute of Physics Series in Plasma Physics. CRC Press, 2004.

D. Block, J. Carstensen, P. Ludwig, W.J. Miloch, F. Greiner, A. Piel, M. Bonitz, and A. Melzer. Wake formation and wake field effects in complex plasmas. *Contributions to Plasma Physics*, 52(10):804–812, 2012. ISSN 1521-3986. doi: 10.1002/ctpp.201200030. URL http://dx.doi.org/10.1002/ctpp.201200030.

L. H. Brace. Langmuir probe measurements in the ionosphere. *Measurement Techniques in Space Plasmas: Particles*, Geophysical Monograph 102, 1998.

H. Bruining. *Physics and Application of Secondary Electron Emission*. Pergamon Press, New York, 1954.

G. Bust, G. Crowley, N. Curtis, A. Reynolds, L. Paxton, C. Coker, and P. Bernhardt. Ida4d-a new ionospheric imaging algorithm using non-linear ground-based and space-based data sources. *American Geophysical Union, Fall Meeting 2007*, 2007.

CubeSat Design Specification Rev. 13. California State Polytechnic University, The CubeSat Program, July 2007.

J. Cazaux. On some contrast reversals in sem: applications to metal/insulator systems. *Ultramicroscopy*, 108:1645–1652, 2008.

F. F. Chen. *Plasma Diagnostic Techniques*. Academic Press, New York, 1965.

F. F. Chen. *Introduction to Plasma Physics and Controlled Fusion*, volume 1. Plenum Press, New York, 2 edition, 1984a.

F. F. Chen. *An Introduction to Plasma Physics*. Plenum Press, New York, 1984b.

F. F. Chen. Langmuir probe diagnostics. Mini-Course on Plasma Diagnostics. IEEE-ICOPS meetin, 2003.

C. D. Child. Discharge from hot cao. *Physical Review*, 32:492–511, 1911.

R. Cimino. Surface related properties as an essential ingredient to e-cloud simulations. *Nuclear Instruments and Methods in Physics Research*, 561:272–275, 2006.

R. Cimino, I. R. Collins, M. A. Furman, M. Pivi, F. Ruggerio, G. Rumulo, and F. Zimmermann. Can low-energy electrons affect high-energy physics accelerators? *Physical Review Letters*, 93(1):14801–14804, 2004.

T. E. Cravens. *Physics of Solar System Plasmas*. Cambridge University Press, Cambridge, 1997.

G. Crowley and M. Pilinski. High latitude ionospheric effects: Observations and modeling. *2013 Space Weather Workshop*, April 2013.

G. Crowley, C. Fish, C. Swenson, G. Bust, A. Barjatya, and M. Larsen. Dynamic ionosphere cubesat experiment october 19, 2010 nsf pi teleconference. October 2010.

G. Crowley, C. Fish, C. Swenson, R. Burt, E. Stromberg, T. Neilsen, S. Burr, A. Barjatya, G. Bust, and M. Larsen. Dynamic ionosphere cubesat experiment (dice). *25th Annual AIAA/USU Conference on Small Satellites*, 2011.

E. H. Darlington and V. E. Cosslett. Backscattering of 0.5-10kev electrons from solid targets. *Journal of Physics D: Applied Physics*, 5:1969–1981, 1972.

L. David. Cubesats: Tiny spacecraft, huge payoffs, September 2004. URL `http://www.space.com/308-cubesats-tiny-spacecraft-huge-payoffs.html`.

A. J. Dekker. *Solid State Physics*. Academic Press, New York, 1958.

T. Dote, H. Amemiya, and T. Ichimiya. Effect of the geomagnetic field on an ionospheric sounding probe. *Journal of Geophysical Research*, 70(2258), 1965.

W.G. Dow and A.F. Reifman. Dynamic probe measurements in the ionosphere. *Physical Review Letters*, 76(987), 1949.

E. Engwall, A. I. Eriksson, and J. Forest. Wake formation behind positively charged spacecraft in flowing tenuous plasmas. *Physics of Plasmas (1994-present)*, 13(6):062904, 2006. doi: http://dx.doi.org/10.1063/1.2199207. URL `http://scitation.aip.org/content/aip/journal/pop/13/6/10.1063/1.2199207`.

C. L. Enloe, D. L. Cooke, W. A. Pakula, M. D. Violet, D. A. Hardy, C. B. Chaplin, R. K. Kirkwood, M. F. Tautz, N. Bonito, G. Roth, G. Courtney, V. A. Davis, M. J. Mandell, D. E. Hastings, G. B. Shaw, G. Giffin, and R. M. Sega. High-voltage interactions in plasma wakes: Results from the charging hazards and wake sutdies (chaws) flight experiments. *Journal of Geophysical Research*, 102(A1):425–433, 1997.

W. M. Farrell, M. L. Kaiser, J. T. Steinberg, and S. D. Bale. A simple simulation of a plasma void: Applications to wind observations of the lunar wake. *Journal of Geophysical*

Research: Space Physics, 103(A10):23653–23660, 1998. ISSN 2156-2202. doi: 10.1029/ 97JA03717. URL http://dx.doi.org/10.1029/97JA03717.

D. C. Ferguson. Ram-wake effects on plasma current collection of the pix 2 langmuir probe. *Spacecraft Environment Interactions Technology*, pages 349–357, 1985.

D. C. Ferguson and G. B. Hillard. Spacecraft charging, arcing, and sustained arcs in low earth orbit. *Progress in Astronautics and Aeronautics*, 237, 2011.

C. Fish, C. Swenson, T. Neilsen, B. Bingham, J. Gunther, G. Crowley, I. Azeem, M. Pilinski, A. Barjatya, and J. Petersen. Dice mission design, development, and implementation: Success and challenges. *26th Annual AIAA/USU Conference on Small Satellites*, 2012.

C. Fish, C. Swenson, G. Crowley, A. Barjatya, T. Neilsen, J. Gunther, I. Azeem, M. Pilinski, R. Wilder, D. Allen, M. Anderson, B. Bingham, K. Bradford, S. Burr, R. Burt, B. Byers, J. Cook, K. Davis, C. Frazier, S. Grover, G. Hansen, S. Jensen, R. LeBaron, J. Martineau, J. Miller, J. Nelsen, W. Nelson, P. Patterson, E. Stromberg, J. Tran, S. Wassom, C. Weston, M. Whiteley, Q. Young, J. Petersen S. Schaire, C. Davis, M. Bokaie, R. Fullmer, R. Baktur, J. Sojka, and M. Cousins. Design, development, implementation, and on-orbit performance of the dynamic ionosphere cubesat experiment mission. *Space Science Reviews*, February 2014.

M. Friedrich, K. M. Torkar, U. P. Hoppe, T. A. Bekkeng, A. Barjatya, and M. Rapp. Multi-instrument comparisons of d-region plasma measurements. *Annales Geophysicae*, 31:135–144, 2013.

T. I. Gombosi. *Physics of the Space Environment*. Cambridge University Press, Cambridge, 1998.

P. Guio and H. L. Pécseli. Phase space structures generated by absorbing obstacles in streaming plasmas. *Annales Geophysicae*, 23(3):853–865, March 2005. URL https:// hal.archives-ouvertes.fr/hal-00317624.

S. R. Gunn and S. Patel. Latex templates, 2014. URL http://www.latextemplates.com/ template/masters-doctoral-thesis.

D. A. Gurnett and A. Bhattacharjee. *Introduction to Plasma Physics with Space and Laboratory Applications*. Cambridge University Press, Cambridge, 2005.

H. Helvajian. *Small Satellites: Past, Present, and Future.* Aerospace Press, El Segundo, CA, 2008.

C. I. Henderson and U. Samir. Observations of the disturbed region around an ionospheric spacecraft. *Planetary and Space Science*, 15:1499–1513, 1967.

A. Jabonski and P. Jiricek. Elastic electron backscattering from surfaces at low energies. *Surface and Interface Analysis*, 24:781–785, 1996.

A. S. Jursa, editor. *Handbook of Geophysics and the Space Environment.* Airforce Systems Command, USAF, 4 edition, 1985.

M. Kanal. Theory of current collection of moving cylindrical probes. *Journal of Applied Physics*, 35(1697), 1964.

S. Kimura and T. Nakagawa. Electromagnetic full particle simulation of the electric field structure around the moon and the lunar wake. *Earth, Planets and Space*, 60(6):591–599, July 2008.

P. T. Kirstein, G. S. Kino, and W. E. Waters. *Space-Charge Flow.* McGraw-Hill, New York, 1967.

H. C. Koons, J. E. Mazur, R. S. Selesnick, J. B. Black, J. F. Fennell, J. L. Roeder, and P. C. Anderson. The impact of space environment on space systems. Aerospace Report TR-99(1670)-1, Aerospace Corporation, El Segundo, CA, July 1999.

S. T. Lai. Spacecraft charging thresholds in single and double maxwellian space environments. *IEEE Transactions on Nuclear Science*, 19:1629–1634, 1991.

S. T. Lai. An improved langmuir probe formula for modeling satellite interactions with near geostationary environment. *Journal of Geophysical Research*, 99:459–468, 1994.

S. T. Lai. The importance of surface conditions for spacecraft charging. *Journal of Spacecraft and Rockets*, in press, 2010.

S. T. Lai. Overview of surface and deep dielectric charging on spacecraft. *Progress in Astronautics and Aeronautics*, 237:1–17, 2011a.

S. T. Lai. *Spacecraft Charging*, volume 237 of *Progess in Astronautics and Aeronautics.* American Institute of Aeronautics and Astronautics, 2011b.

S. T. Lai. *Fundamentals of Spacecraft Charging: Spacecraft Interactions with Space Plasmas*. Princeton University Press, 1 edition, 2012.

M. Lampe, G. Joyce, and G. Ganguli. Structure and dynamics of dust in streaming plasma: dust molecules, strings, and crystals. *Plasma Science, IEEE Transactions on*, 33(1):57–69, Feb 2005. ISSN 0093-3813. doi: 10.1109/TPS.2004.841926.

I. Langmuir. The effect of space charge and residual gases on thermionic currents in high vacuum. *Physical Review*, 2:450–486, 1913.

I. Langmuir. *Collected Works of Irving Langmuir*. Pergamon Press, New York, 1960.

Y. Lin and D. G. Joy. A new examination of secondary electron yield data. *Surface and Interface Analysis*, 37:895–900, 2005.

S. A. Maiorov, S. V. Vladimirov, and N. F. Cramer. Plasma kinetics around a dust grain in an ion flow. *Phys. Rev. E*, 63:017401, Dec 2000. doi: 10.1103/PhysRevE.63.017401. URL http://link.aps.org/doi/10.1103/PhysRevE.63.017401.

L. M. Martinez. Analysis of leo radiation environment and its effects on spacecraft's critical electronic devices. Master's thesis, Embry-Riddle Aeronautical University, December 2011.

F. Melandsø and J. Goree. Polarized supersonic plasma flow simulation for charged bodies such as dust particles and spacecraft. *Phys. Rev. E*, 52:5312–5326, Nov 1995. doi: 10.1103/PhysRevE.52.5312. URL http://link.aps.org/doi/10.1103/PhysRevE.52.5312.

R. L. Merlino. Understanding langmuir probe current-voltage characteristics. *American Journal of Physics*, 75(12), December 2007.

W. J. Miloch, J. Trulsen, and H. L. Pécseli. Numerical studies of ion focusing behind macroscopic obstacles in a supersonic plasma flow. *Phys. Rev. E*, 77:056408, May 2008a. doi: 10.1103/PhysRevE.77.056408. URL http://link.aps.org/doi/10.1103/PhysRevE.77.056408.

W. J. Miloch, S. V. Vladimirov, H. L. Pécseli, and J. Trulsen. Wake behind dust grains in flowing plasmas with a directed photon flux. *Phys. Rev. E*, 77:065401, Jun 2008b. doi: 10.1103/PhysRevE.77.065401. URL http://link.aps.org/doi/10.1103/PhysRevE.77.065401.

W. J. Miloch, T. A. Bekkeng, and T. Lindem. Charging and performance of the cubestar satellite studied by numerical simulations. In *39th COSPAR Scientific Assembly*, volume 39 of *COSPAR Meeting*, page 1240, July 2012a.

W. J. Miloch, V. V. Yaroshenko, S. V. Vladimirov, H. L. Pecseli, and J. Trulsen. Spacecraft charging in flowing plasma; numerical simulations. In *Journal of Physics: Conference Series*, volume 370. 14th Latin American Workshop on Plasma Physics (LAWPP 2011), IOP Publishing Ltd, 2012b.

R. Mitharwal. A two-dimensional numerical simulation of plasma wake structure around a cubesat. Master's thesis, Utah State University, 2011.

H. M. Mott-Smith and I. Langmuir. The theory of collectors in gaseous discharges. *Physical Review*, 28(727), 1926.

G. Murphy, J. Pickett, N. Dangelo, and W. S. Kurth. Measurements of plasma parameters in the vicinity of the space shuttle. *Planetary and Space Science*, 34(1):993–1004, October 1986.

Annual Report- National Science Foundation (NSF) CubeSat-Based Science Missions for Geospace and Atmospheric Research, October 2013. National Science Foundation (NSF), NASA.

K. W. Ogilvie, J. T. Steinberg, R. J. Fitzenreiter, C. J. Owen, A. J. Lazarus, W. M. Farrell, and R. B. Torbert. Observations of the lunar plasma wake from the wind spacecraft on december 27, 1994. *Geophysical Research Letters*, 23(10):1255–1258, 1996. ISSN 1944-8007. doi: 10.1029/96GL01069. URL http://dx.doi.org/10.1029/96GL01069.

E. Oz. *Physics of Particle Trapping in Ultrarelativistic Plasma Wakes*. PhD thesis, University of Southern California, 2007.

S. M. Prokopenko and J. G. L. Laframboise. High voltage differential charging of geostationary spacecraft. *Journal of Geophysical Research*, 85(A8):4125–4131, 1980.

W. J. Raitt, D. E. Siskind, P. M. Banks, and R. R. Williamson. Measurements of the thermal plasma environment of the space shuttle. *Planetary and Space Science*, 32(1): 457–467, 1984.

K. U. Riemann. The bohm criterion and sheath formation. *Journal of Physics D: Applied Physics*, 24(1991):493–518, 1990.

F. Rogier and D. Volpert. Poisson solver documentation. SPIS supplementary material.

U. Samir, R. Gordon, L. Brace, and R. Theis. The near wake structure of the atomospheric explorer c (ae-c) satellite: A parametric investigation. *Journal of Geophysical Research*, 84:513–522, 1979.

U. Samir, N. H. Stone, and K. H. Wright. On plasma disturbances caused by the motion of the space shuttle and small satellites- a comparison of in situ observations. *Journal of Geophysical Research*, 91:277–285, January 1986.

U. Samir, R. H. Comfort, K. H. Wright, and N. H. Stone. Intercomparison among plasma wake models for plasmapheric and ionospheric conditions. *Planetary and Space Science*, 35:1477– 1487, 1987.

N. L. Sanders and G. T. Inouye. *Secondary emission effects on spacecraft charging: energy distribution consideration*. Number ADA-084626. NASA-2071, Air Force Geophysics Laboratory, Hanscom AFB, MA, 1978.

J. J. Scholtz, D. Dijkkamp, and R. W. A. Schmitz. Secondary electron properties. *Philips Journal of Research*, 50(3-4):375–389, 1996.

V. A. Schweigert, I. V. Schweigert, A. Melzer, A. Homann, and A. Piel. Alignment and instability of dust crystals in plasmas. *Phys. Rev. E*, 54:4155–4166, Oct 1996. doi: 10. 1103/PhysRevE.54.4155. URL http://link.aps.org/doi/10.1103/PhysRevE.54.4155.

E. Séran, J.-J. Berthelier, F. Z. Saouri, and J.-P. Lebreton. The spherical segmented langmuir probe in a flowing thermal plasma: numerical model of the current collection. *Annales geophysicae*, 23:1723–1733, July 2005.

R. W. Shunk and A. F. Nagy. *Ionospheres: Physics, Plasma Physics, and Chemistry*. Cambridge University Press, 2 edition, 2009.

N. Singh, U. Samir, K. H. Wright, and N. H. Stone. A possible explanation of the electron temperature enhancement in the wake of a satellite. *Journal of Geophysical Research*, 92: 6100–6106, 1987.

D. E. Siskind, W. J. Raitt, P. M. Banks, and P. R. Williamson. Interactions between the orbiting space shuttle and the ionosphere. *Planetary and Space Science*, 32:881–896, 1984.

G. Sookahet. Spacecraft plasma interaction analysis and simulation toolkit: Gmsh user tutorial for cad and meshing. Technical report, ONERA and Artenum and University Paris 7, 2003.

E. J. Sternglass. Theory of secondary electron emission. Scientific paper 1772, Westinghouse Research Laboratories, Pittsburgh, PA, 1954a.

E. J. Sternglass. Backscattering of kilovolt electrons from solids. *Physical Review*, 95:345–358, 1954b.

N. H. Stone and C. Bonifazi. The tss-1r mission: Overview an scientific context. *Geophysical Research Letters*, 25(4):409–412, 1998.

E. Stromberg. Dice cubesat mission. Spring 2011 CubeSat Workshop, April 2011.

D. M. Suszynsky and J. E. Borovsky. Modified sternglass theory for the emission of secondary electrons by fast-electron impact. *Physical Review*, 45(9):6424–6429, 1992.

B. Thiebault, B. Jeanty-Ruard, and J. Forest. Spis-geo user manual. Technical report, Artenum, Paris, 2013.

S. V. Vladimirov, S. A. Maiorov, and N. F. Cramer. Dynamics of the charging and motion of a macroparticle in a plasma flow. *Phys. Rev. E*, 63:045401, Mar 2001. doi: 10.1103/ PhysRevE.63.045401. URL `http://link.aps.org/doi/10.1103/PhysRevE.63.045401`.

E. C. Whipple. Potentials of surfaces in space. *Reports on Progress in Physics*, 44(11):1197, 1981.